ACS NANO

www.acsnano.org

ARTICLE

Concurrent Detection of Protein and miRNA at the Single Extracellular Vesicle Level Using a Digital Dual CRISPR-Cas Assay

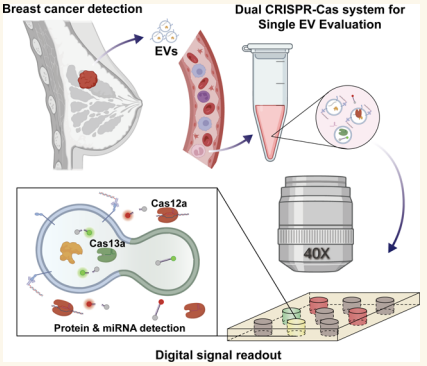
Xun Xu,[▽] Yuanyue Zhang,[▽] Jiajia Liu, Shujin Wei, Nan Li, Xintong Yao, Muxue Wang, Xiaohan Su, Gaoshan Jing, Junquan Xu, Yan Liu, Ying Lu, Jing Cheng,* and Youchun Xu*

Cite This: *ACS Nano* 2025, 19, 1271−1285

Read Online

ACCESS | Metrics & More | Article Recommendations | Supporting Information

ABSTRACT: The simultaneous detection of proteins and microRNA (miRNA) at the single extracellular vesicle (EV) level shows great promise for precise disease profiling, owing to the heterogeneity and scarcity of tumor-derived EVs. However, a highly reliable method for multiple-target analysis of single EVs remains to be developed. In this study, a digital dual CRISPR-Cas-powered Single EV Evaluation (ddSEE) system was proposed to enable the concurrent detection of surface protein and inner miRNA of EVs at the single-molecule level. By optimizing simultaneous reaction conditions of CRISPR-Cas12a and CRISPR-Cas13a, the surface protein of EVs was detected by Cas12a using antibody-DNA conjugates to transfer the signal of the protein to DNA, while the inner miRNA was analyzed by Cas13a through EV-liposome fusion. A microfluidic chip containing 188,000 microwells was used to convert the CRISPR-Cas system into a digital assay format to enable the absolute quantification of miRNA/protein-positive EVs without bias through fluorescence imaging, which can detect as few as 214 EVs/μL. Finally, a total of 31 blood samples, 21 from breast cancer patients and 10 from healthy donors, were collected and tested, achieving a diagnostic accuracy of 92% in distinguishing patients with breast cancer from healthy donors. With its absolute quantification, ease of use, and multiplexed detection capability, the ddSEE system demonstrates its great potential for both EV research and clinical applications.



KEYWORDS: *CRISPR-Cas, single molecule, single EV, microwell, liposome*

Downloaded via UNIV OF CALIFORNIA DAVIS on January 18, 2025 at 01:14:06 (UTC).
See https://pubs.acs.org/sharingguidelines for options on how to legitimately share published articles.

Extracellular vesicles (EVs) are the most intriguing targets for liquid biopsies because of their stable encapsulation of various biological molecules, including proteins, nucleic acids, metabolites, and lipids, that can reflect their origin in tumor cells.[1] However, the generation of EVs from tumors, blood cells, and platelets contributes to creating a diverse and complex population of EVs in the bloodstream. This diversity, along with the scarcity of tumor-derived EVs, complicates their precise characterization.[2−4]

Currently, traditional methods for EV marker detection, such as immunoblotting, enzyme-linked immunosorbent assay (ELISA), mass spectrometry, flow cytometry, and quantitative polymerase chain reaction (qPCR), are time-consuming, labor-intensive, and relatively insensitive.[5,6] These traditional EV analysis approaches can provide only generalized insights into large-volume samples and struggle to distinguish tumor cell-specific EVs from background EVs. Furthermore, the inherent heterogeneity of EVs, even those secreted from a single cell, highlights the importance of technologies capable of dissecting potential tumor biomarkers at the single EV level.[7]

To realize the single EV detection, methods such as high-resolution flow cytometry, surface-enhanced Raman spectroscopy, and digital ExoELISA[6,8] have been proposed; however, a common limitation is that only one type of EV biomarker can be analyzed. For multiple-target analysis of individual EVs, most efforts have focused on identifying multiple surface proteins.[9−12] Detecting internal microRNAs (miRNAs) in a single EV is challenging because of their scarcity (the average number of miRNAs per EV is less than one copy) and location (miRNAs are enclosed within EVs).[2,13] Recent studies[14,15] have utilized molecular beacons and fluorescently labeled antibodies in conjunction with total internal reflection fluorescence microscopy to analyze the surface proteins and inner miRNAs of EVs at

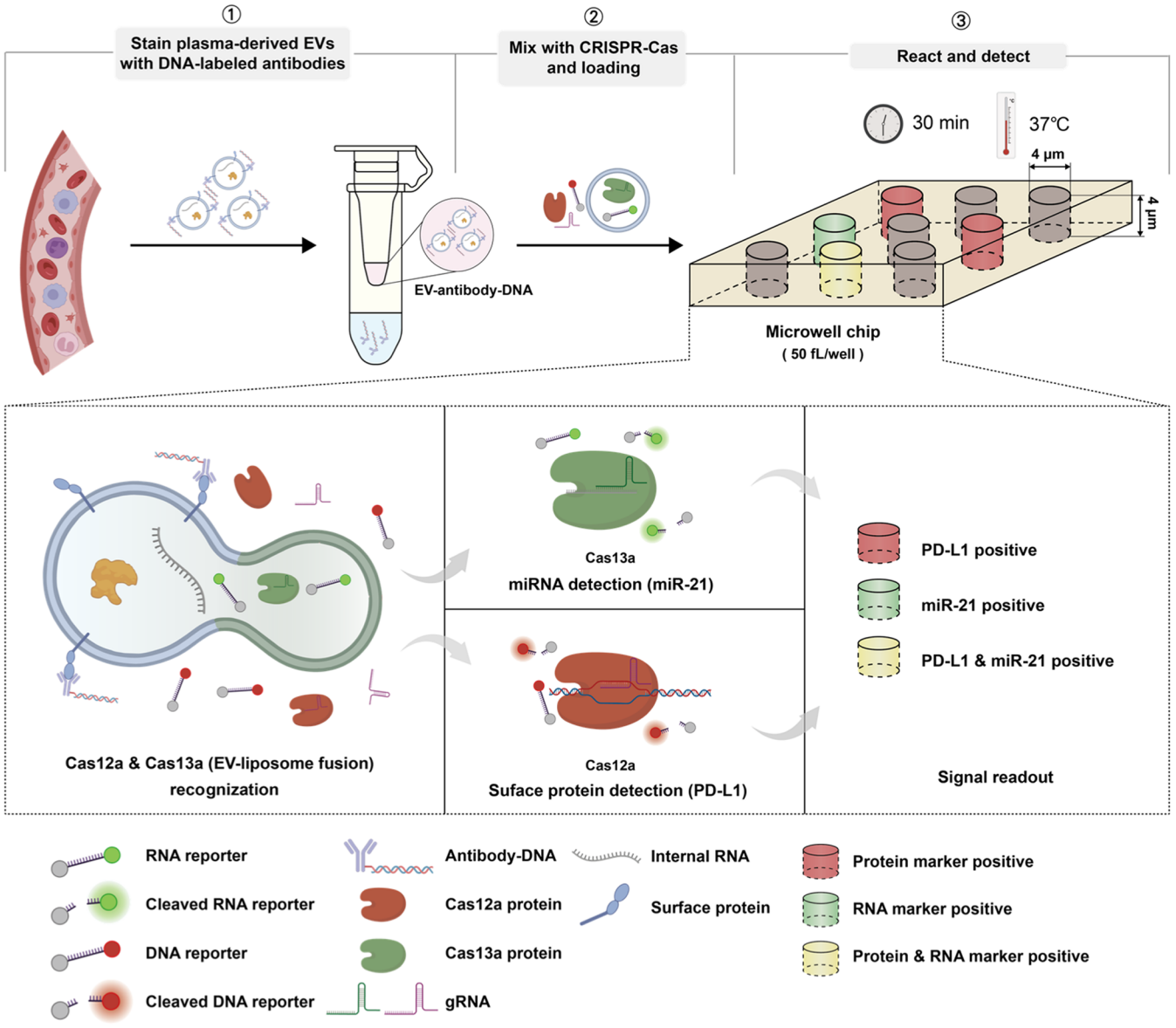
Received: September 26, 2024
Revised: December 2, 2024
Accepted: December 9, 2024
Published: December 17, 2024



© 2024 American Chemical Society

https://doi.org/10.1021/acsnano.4c13557
ACS Nano 2025, 19, 1271−1285

Scheme 1. Concept of the ddSEE System[a]



[a]Antibody-DNA-labeled EVs were prepared *via* incubation with antibody-DNA complexes and ultrafiltration to remove free antibody-DNA conjugates. The prepared EV-antibody-DNA complexes were subsequently mixed with Cas12a reagents and Cas13a reagents encapsulated in liposomes, and then loaded into a microwell array chip for compartmentalization. In each individual microwell, EV-liposome fusion facilitated the delivery of Cas13a reagents into EVs to detect the inner miRNA and cleave RNA reporters (green fluorescence), while the corresponding antibody-DNA complexes activated Cas12a to detect a specific protein and cleave DNA reporters (red fluorescence).

high magnification. However, these methods lack a signal amplification step, making them susceptible to false positives typically observed in single-molecule detection. Moreover, molecular beacons are unstable in aqueous solutions, contributing to high background noise during detection.[16,17] Therefore, reliable and easy-to-use methods that can conveniently and accurately analyze the surface protein and inner miRNA of single EVs are still lacking.

Since the pioneering work on CRISPR-Cas-based molecular diagnosis by Zhang in 2017,[18] the CRISPR-Cas system has been widely applied for the nucleic acid-based detection of pathogens,[18−20] such as SARS-CoV-2, and has been further developed to use aptamers or antibody-DNA conjugates to convert protein signals into DNA signals, enabling CRISPR-Cas to detect proteins, toxins, and other molecules.[21−24] These advancements have significantly expanded the range of detectable targets by the CRISPR-Cas system. However, due to the inherent limitations of CRISPR-Cas detection capabilities, current assays often require preamplification steps such as recombinase polymerase amplification (RPA), loop-mediated isothermal amplification (LAMP), and polymerase chain reaction (PCR) before CRISPR-Cas reactions to enhance the signals. These additional steps not only increase reaction time and cost but also pose a risk of contamination due to the nucleic acid amplification process. Recent efforts have confined the CRISPR-Cas system to microchambers, enabling the amplification-free detection of DNA using Cas12a or miRNA using Cas13a.[25−27] Inspired by these advancements, we propose a **d**igital **d**ual CRISPR-Cas-powered **S**ingle **E**V **E**valuation (**ddSEE**) system for the highly sensitive and concurrent

https://doi.org/10.1021/acsnano.4c13557
ACS Nano 2025, 19, 1271−1285

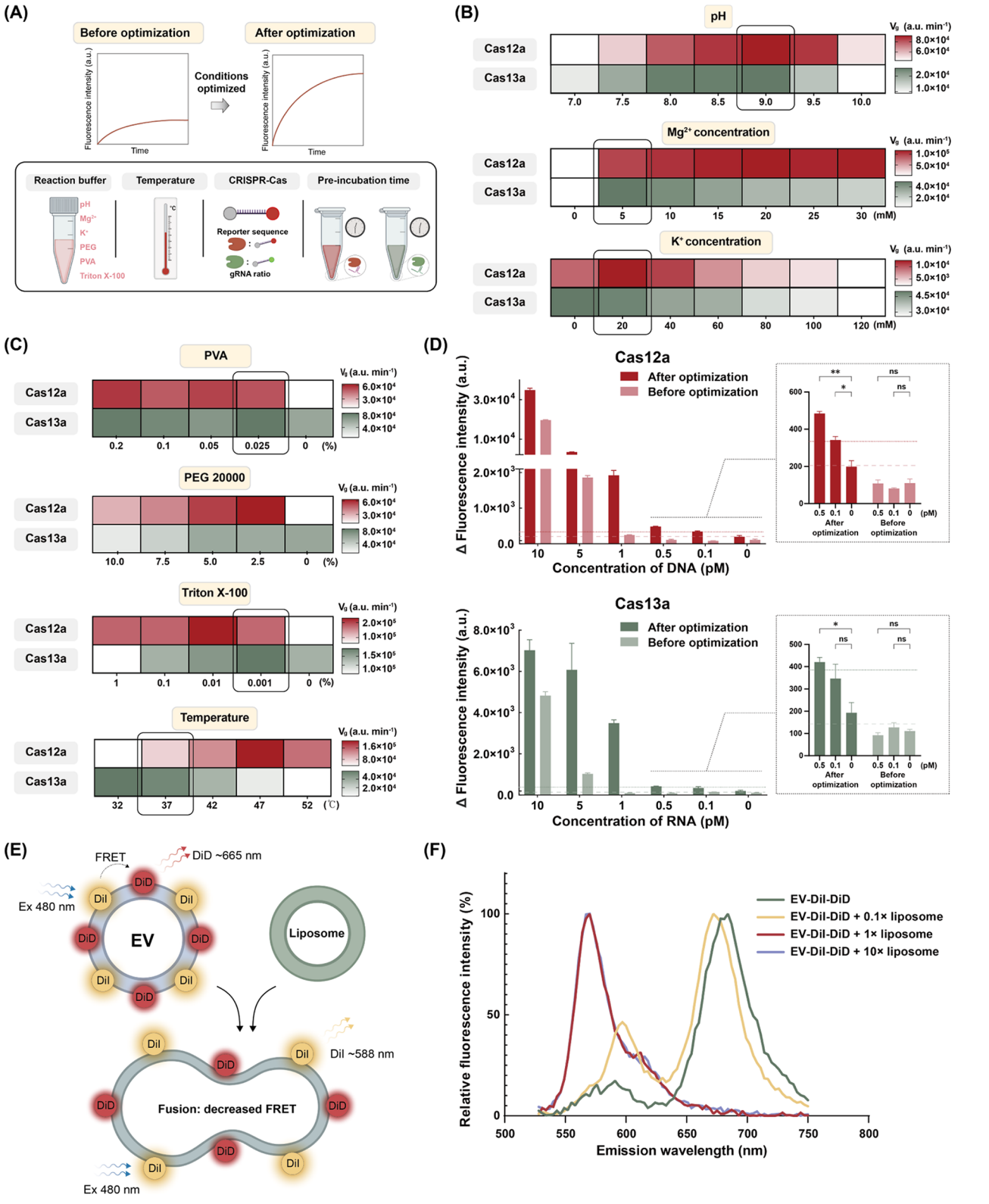


Figure 1. Optimization of reaction conditions for the dual CRISPR-Cas assay. (A) Schematic of the dual CRISPR-Cas assay optimization, including systematic evaluation of buffer compositions, pH, reaction temperature, reporter sequence, gRNA-to-Cas protein ratio, and preincubation time. (B) Assessment of Cas13a/Cas12a assay efficiency under various pH values and cation concentrations (Mg^{2+} and K^{+}). (C) Effect of additives and temperature on Cas13a/Cas12a assay efficiency. The fluorescence growth rate (V_g) is calculated as $V_g = \Delta F/\Delta t$. (D) Fluorescence changes in Cas12a and Cas13a with conventional NEB 2.1 buffer versus optimized buffer at different target concentrations. The horizontal dashed line indicates the detection limit before optimization, while the dotted line shows the detection limit after optimization, calculated as the mean of the NTC plus standard error ×3. (E, F) Measurement of the increased Förster resonant energy transfer (FRET) donor signal (588 nm) and the decreased acceptor signal (665 nm) on the labeled EVs after membrane fusion with unlabeled liposomes.

https://doi.org/10.1021/acsnano.4c13557
ACS Nano 2025, 19, 1271−1285

detection of proteins and miRNA in single EVs. To build this system, optimal conditions for the concurrent reaction of the CRISPR-Cas12a and CRISPR-Cas13a systems were first screened for the simultaneous detection of DNA and miRNA in microwells at the single-molecule level. Antibodies targeting the surface protein of EVs were labeled with a DNA oligo to transfer protein detection to CRISPR-Cas12a-based DNA detection. Then, the CRISPR-Cas13a system was encapsulated in a liposome to detect the inner miRNA of EVs through EV-liposome fusion. The use of liposomes to deliver reagents allows for the detection of RNA encapsulated within EVs without the need for EV lysis and RNA purification.[28] Finally, the ddSEE system was applied to detect EVs from plasma samples of 21 patients with breast cancer (BC) and 10 healthy donors (HD). By evaluating the co-occurrence of the PD-L1 protein and miR-21 at the single EV level, a diagnostic accuracy of 92% was obtained, distinguishing BC samples from HD samples. This system can potentially serve as a tool for the multiplexed, simultaneous detection of disease-specific EV surface protein and internal molecular cargo in clinical settings within 2.5 h, thereby improving the clinical applicability of EV-based liquid biopsy.

RESULTS

Workflow of the ddSEE System. Digital microwell/droplet-based assays have been widely used for the division and precise profiling of individual molecules or cells because of their cost efficiency, scalability, and compatibility with imaging.[29−32] Using this compartmentalization strategy, ddSEE was performed within a microwell array chip to achieve segregation and the simultaneous detection of protein and miRNA in individual EVs.

The ddSEE workflow was divided into three essential steps (Scheme 1). First, enriched EVs derived from plasma were incubated with DNA-labeled antibodies, converting protein signals to DNA signals, followed by ultrafiltration to remove unbound antibody-DNA complexes. Second, EV-antibody-DNA complexes were mixed with a CRISPR-Cas12a mixture and liposomes encapsulating the CRISPR-Cas13a mixture.[33−36] Third, this whole mixture was loaded into a microwell array chip and incubated at 37 °C, where single EVs were distributed into individual microwells via Poisson distribution. At this stage, DNA corresponding to the surface proteins of EVs activated Cas12a, whereas the miRNA inside EVs activated Cas13a, which was delivered via EV-liposome fusion. Once activated, Cas12a cleaved DNA reporters (with red fluorophores) with catalytic efficiency ranging from approximately 3.2×10^6 to 1.7×10^9 M^{-1} s^{-1},[20,37−39] whereas Cas13a cleaved RNA reporters (with green fluorophores) with catalytic efficiency about 3.7×10^6 to 3.2×10^8 M^{-1} s^{-1}.[39−42] The specific values may vary depending on factors such as the gRNA and reporter sequences as well as other reaction conditions. Such high efficiency of the CRISPR-Cas system in continuously cleaving the surrounding reporters resulted in an accumulation of high-yield fluorescent signals in a small volume (50 fL) within 30 min, which can easily illuminate the microwells (4 μm in diameter, 4 μm in depth) of the microfluidic chip used in this study (Figure S1A,B). Moreover, the simplicity of the digital dual CRISPR-Cas assay, together with the imaging-friendly features of the microwell array chip, simplified the entire workflow to allow for the *in situ* detection of single EVs. All of these enabled the concurrent detection of surface protein and inner miRNA in single EVs at single-molecule resolution.

Refinement of the Reaction Conditions for the Dual CRISPR-Cas Assay. Despite the widespread use of Cas12a and Cas13a in DNA and RNA detection assays, most of these methods have been preceded by nucleic acid amplification techniques.[43,44] The potential of integrating orthogonal Cas12a and Cas13a in a single signal accumulation reaction without nucleic acid amplification for concurrent detection of DNA and RNA remains largely unexplored. Considering that both Cas12a and Cas13a can react under physiological conditions[45] and require the same divalent metal ions, such as Mg^{2+}, as cofactors to exert their enzymatic activity,[46,47] it is theoretically feasible to integrate Cas12a and Cas13a into a single reaction system for the simultaneous detection of DNA and RNA. Accounting for the different pH preferences of various Cas enzymes, we used LbaCas12a and LbuCas13a in this study, which are both widely used and favor alkaline conditions in our concurrent reaction system. To quantitatively assess the trans-cleavage activities of LbaCas12a and LbuCas13a in different conditions, the fluorescence growth rate V_g was calculated as follows:

$$V_g = \Delta F / \Delta t$$

where ΔF denotes the change in fluorescence intensity and Δt represents the first 3 min.[25]

We then screened various reaction buffers, including several commercially available options and those documented in the literature, to significantly enhance the enzymatic activity of Cas proteins (Table S1).[25,48] Eventually we found that HOLMES Buffer 1 was the most effective buffer for the concurrent reaction of Cas12a and Cas13a (Figure S2). However, the activities of Cas12a and Cas13a in the HOLMES Buffer 1 were still insufficient for single-molecule detection in our microwell array chip. Therefore, further optimization based on HOLMES Buffer 1 was performed by fine-tuning the pH, components, and additives of the reaction buffer (Figure 1A). First, spermidine in HOLMES Buffer 1 was excluded because it inhibited Cas13a activity (Figure S3A,B). As most papers reported peak trans-cleavage activity for LbaCas12a in mildly alkaline conditions,[25,48−50] pH values ranging from 7.0 to 10.0 (in 0.5 increments) were investigated. We noticed that Cas12a and Cas13a exhibited the highest cleavage rates at pH 9.0. Next, the concentrations of metal ions (Mg^{2+} and K^+) were modified, revealing that 5 mM $MgCl_2$ and 20 mM KCl were the optimal conditions for the reaction (Figure 1B). Subsequently, three types of additives were examined. First, poly(vinyl alcohol) (PVA) and polyethylene glycol (PEG), which are often used as scaffolds for enzymatic reactions, were added to the reaction buffer. PVA significantly promoted the reaction efficiencies of Cas12a and Cas13a, similar to PEG 20000 (Figure 1C, Figure S4); however, it introduced less background noise than PEG 20000 (Figure S5A,B). Next, surfactants such as Triton X-100 have been reported to improve the efficiency of the CRISPR-Cas reaction (Figure 1C, Figure S6C)[48] and also pose a risk of EV lysis.[51] Therefore, the effects of varying concentrations of Triton X-100 on EVs were quantitatively assessed by using nanoparticle tracking analysis (NTA). Our data revealed that when the Triton X-100 concentration ≥0.1% (w/v), there was a pronounced reduction in EV concentration, which was attributed to EV lysis (Figure S6A,B). Consequently, a lowered concentration for Triton X-100 (0.001%) was selected to avoid EV lysis before the sample was loaded into the chip. Finally, PCR-grade bovine serum albumin (BSA) was incorporated into the system to minimize the potential adsorption of enzymes onto the chip.[50]

https://doi.org/10.1021/acsnano.4c13557
ACS Nano 2025, 19, 1271−1285

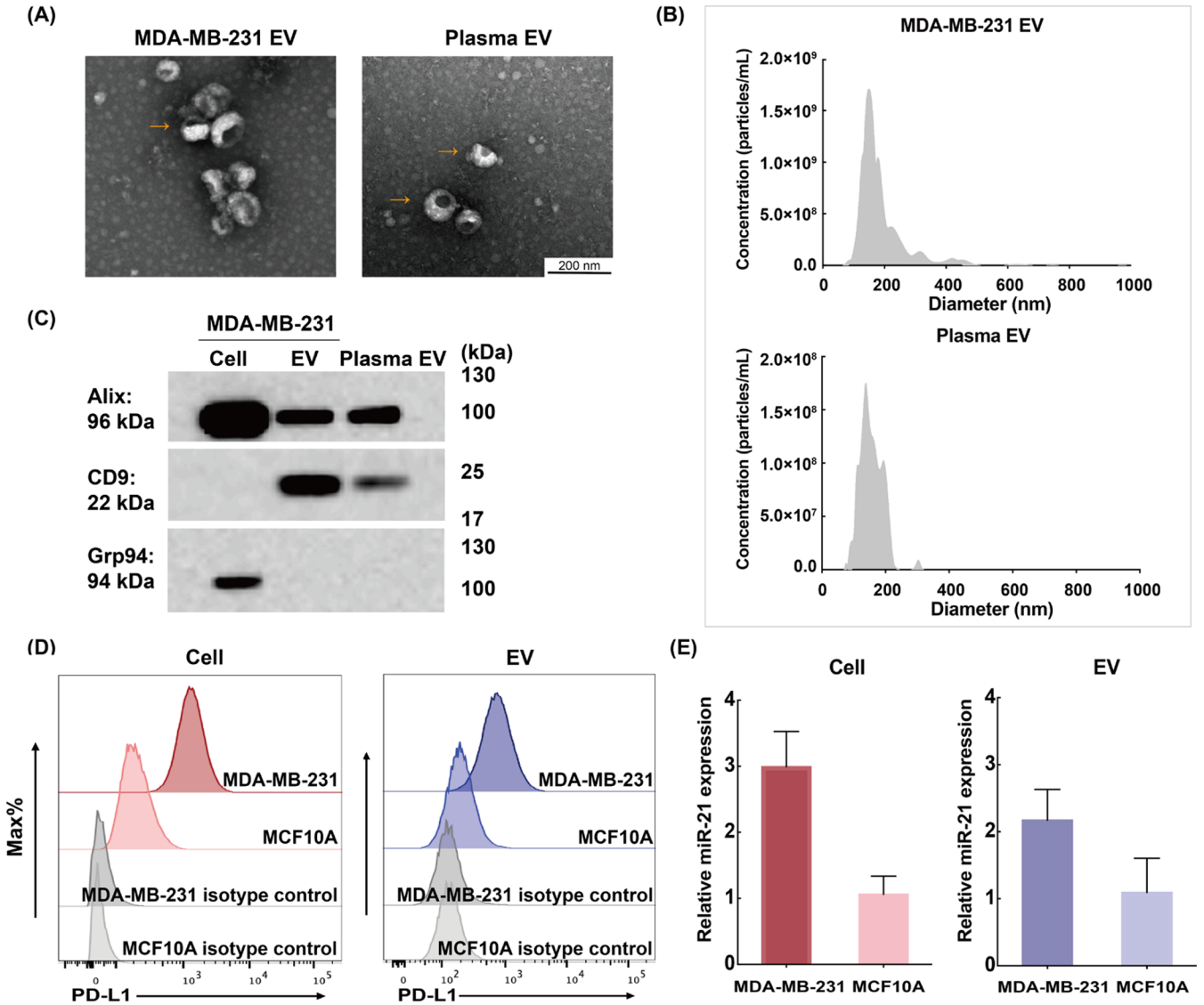


Figure 2. Characterization of EVs. (A) Representative TEM images of EVs isolated from the MDA-MB-231 cell culture medium and plasma. (B) Size distribution of EVs isolated from the MDA-MB-231 cell culture medium and plasma. (C) Western blotting images showed the expression of the positive EV protein markers ALIX, CD9, and the negative protein marker Grp94 in MDA-MB-231 cells, EVs derived from MDA-MB-231 cells and plasma. (D) Flow cytometry analysis of the expression of PD-L1 on the membranes of cells and EVs. CD63-conjugated beads were utilized to capture the EVs. Beads conjugated with IgG served as an isotype negative control in each experiment. (E) miR-21 expression in MDA-MD-231 cells, MCF10A cells, MDA-MD-231-derived EVs, and MCF10A-derived EVs were determined using RT-qPCR. Relative miRNA expression levels were normalized against that of snoU6. The data are presented as fold changes relative to the control. All experiments were repeated at least three times. Error bars represent the mean ± standard error of the mean (SEM) of three repeated experiments.

After refining the composition of the reaction buffer, other factors that may influence the reaction activities of Cas12a and Cas13a were also examined, including the reporter sequence, reaction temperature, the ratio of gRNA to the Cas enzyme, and preincubation time (Figure 1A). First, the literature presented varying findings, with some studies suggesting that C-rich substrates were more susceptible to cleavage, while others favored TA-rich substrates.[25,52] Through an extensive comparison of various reporters differing in sequence and length, a 10-bp substrate was selected based on its superior efficiency in Cas12a-mediated cleavage (Figure S7). Second, the reaction temperature is a common influencing factor for Cas12a and Cas13a reactions. An increase in temperature may enhance enzyme−substrate interactions due to increased kinetic energy, but exceeding the optimum temperature can distort the enzyme's active site and inhibit the formation of enzyme−substrate complexes. Therefore, a comparative analysis of the reaction rates of Cas12a and Cas13a was conducted at temperatures ranging from 32 to 52 °C in increments of 5 °C. It was found that Cas12a preferred slightly higher temperatures, while Cas13a showed optimal activity at the physiological temperature of 37 °C. To achieve the balanced performance of Cas12a and Cas13a activity, we selected 37 °C as the temperature for the concurrent reaction (Figure 1C). Finally, the ratio of gRNA to Cas enzyme was examined, and the preincubation time for gRNA with Cas12a/Cas13a was optimized. For Cas12a, the highest cleavage efficiency was observed when the ratio of gRNA to Cas enzyme was 2:1; extending the incubation time did not yield any additional benefits. For Cas13a, higher ratios of gRNA to Cas enzyme and

https://doi.org/10.1021/acsnano.4c13557
ACS Nano 2025, 19, 1271−1285

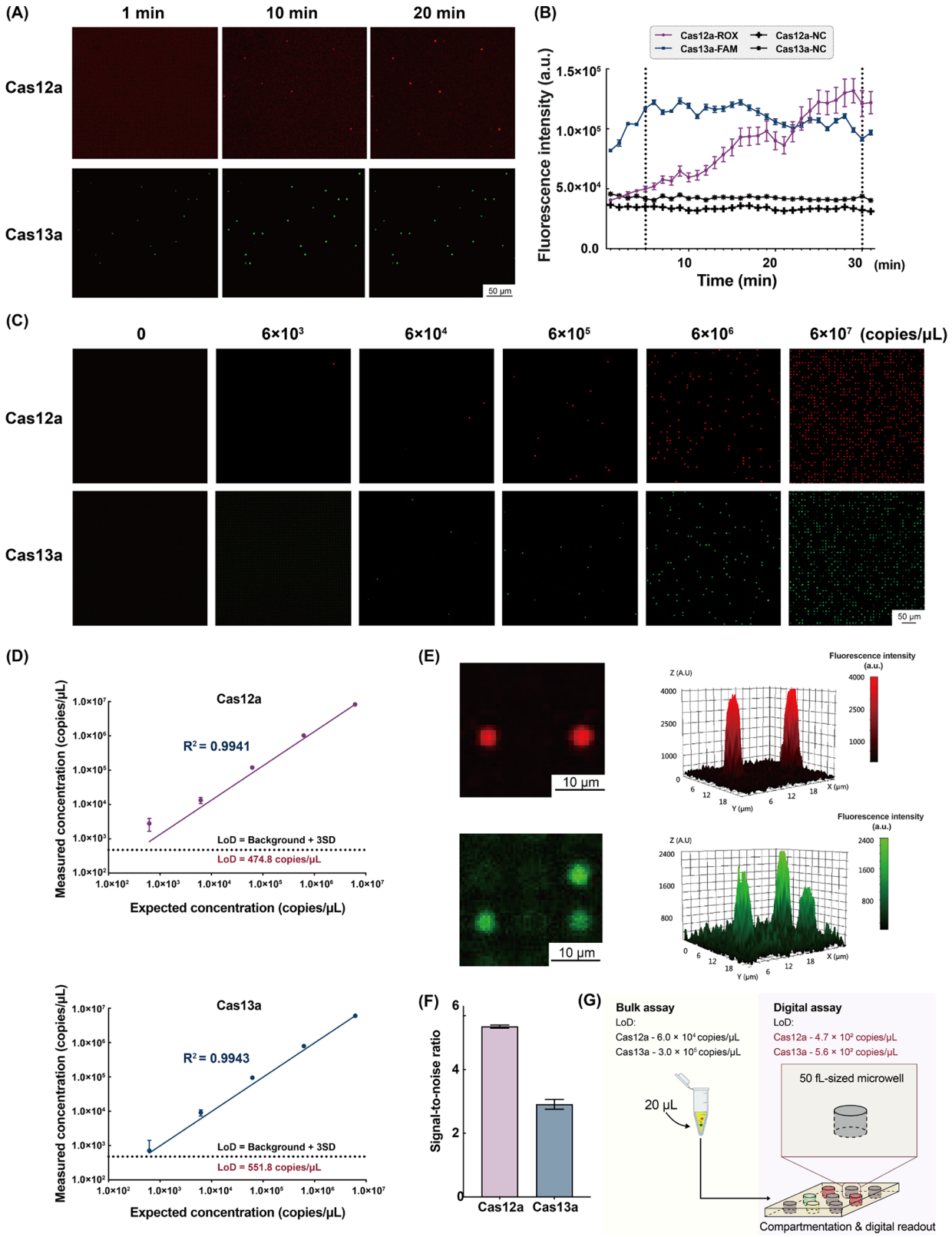


Figure 3. Performance of the digital dual CRISPR-Cas assay. (A) Fluorescence images of microwells captured at 40× magnification after different incubation times. (B) Real-time fluorescence curves of the positive microwells. The fluorescence growth curves of the positive wells were normalized against the decline in background fluorescence signals from the negative microwells. (C) End point fluorescence images of the digital dual CRISPR-Cas assay using miRNA/DNA templates at various concentrations. (D) Quantification range of the digital dual CRISPR-Cas assay. (E) Representative images of single-molecule detection using Cas12a and Cas13a within microwells. (F) SBR (signal-to-background ratio) of the fluorescence intensity from the positive microwell to the negative microwell across three random fields of view. (G) Comparison of the LoD between the digital dual CRISPR-Cas assay and the corresponding bulk assay, where the copies/μL for the bulk reaction were estimated from the detection limit of 100 fM for Cas12a and 500 fM for Cas13a.

https://doi.org/10.1021/acsnano.4c13557
ACS Nano 2025, 19, 1271−1285

longer incubation times correlated with enhanced cleavage efficiency. For maximum efficiency, the optimal ratio of gRNA to Cas enzyme for Cas13a was 1:8, with a 30 min preincubation at 37 °C (Figure S8A,B).

Overall, through the above-mentioned optimization procedures, an optimal solution composed of 5 mM $MgCl_2$, 20 mM KCl, 40 mM Tris-HCl (pH 9.0), 0.001% Triton X-100, 1 mM DTT, 100 μg/mL BSA, and 0.025% PVA, termed the "dual CRISPR-Cas buffer", was obtained. The other conditions for the concurrent reaction of Cas12a and Cas13a are listed in Table S2. Under these optimized conditions, the detection limit of the CRISPR-Cas system improved 10-fold compared to the extensively used commercial NEB 2.1 buffer, enabling the sensitive detection of target molecules in tubes at concentrations as low as 100 fM for Cas12a and 500 fM for Cas13a (Figure 1D). Finally, we optimized the EV-to-liposome fusion ratio. EVs were dual-labeled with DiI (donor) and DiD (acceptor) dyes to confirm fusion using a Förster resonant energy transfer (FRET) dequenching assay.[35,53] Increasing the liposome/EV ratio led to decreased FRET activity and enhanced donor signal, indicating dye dilution by the liposome membrane. Complete fusion of EVs and liposomes was observed at both 10× and 1× liposome conditions, with consistent decreases in FRET activity (Figure 1E,F). Based on these results, we selected the 1× liposome condition for further experiments.

Characterization of EVs. EVs from the culture medium of the BC cell line MDA-MB-231 and plasma were isolated via ultracentrifugation, and their morphology, size distribution, and protein markers were characterized according to the MISEV 2024 guidelines.[54] Transmission electron microscopy (TEM) revealed typical EV structures in EVs derived from cell line supernatants and plasma (Figure 2A). Furthermore, NTA revealed that EVs from the cell culture medium had a peak particle diameter of 142 nm (Figure 2B), whereas plasma-derived EVs exhibited a peak particle diameter of 130 nm. Immunoblotting of EV lysates revealed the presence of EV marker CD9, a member of the tetraspanin family, primarily in the EV fraction with minimal detection in the cellular fraction (Figure 2C). Additionally, the high expression of ALIX, which is involved in ALIX- and ESCRT-III-dependent pathways for tetraspanin sorting and delivery to EVs, was observed in isolated EVs, further confirming their identity. In contrast, Grp94, a marker of the endoplasmic reticulum, was exclusively detected in the cellular fraction, but not in the EVs, indicating the absence of cell or apoptotic body contamination in the EV samples. Collectively, these results confirmed the successful isolation of EVs from MDA-MB-231 culture medium and plasma.

In the present study, two crucial cancer biomarkers present in EVs, PD-L1 and miR-21, were measured.[55−58] The PD-L1 protein promotes tumor progression and facilitates evasion of the immune system by inhibiting PD-1 on immune cells. Meanwhile, miR-21, which is overexpressed in many types of cancer, promotes tumor growth and predicts a poor prognosis. Detecting these markers in EVs aids cancer diagnosis, understanding cancer mechanisms, and guiding personalized treatments. Flow cytometry analysis revealed that PD-L1 was highly expressed in the BC cell line MDA-MB-231; its expression was lower in the normal mammary epithelial cell line MCF10A (Figure 2D, Figure S9A). Similarly, we measured the expression levels of miR-21 using qPCR, calculating the relative expression separately for cell samples and EV samples, as detailed in the Methods section. The results showed that the expression of miR-21 in MDA-MB-231 cells was 3-fold higher than that in MCF10A cells. Correspondingly, EVs secreted by MDA-MB-231 cells exhibited significantly higher levels of PD-L1 and double the amount of miR-21 compared with EVs secreted by MCF10A cells (Figure 2E, Figure S9B). However, owing to the complexity of tumors, single-target detection fails to achieve high sensitivity and specificity for clinical cancer diagnosis.[59−61] Therefore, we attempted to detect the concurrence of different biomarkers, specifically protein and miRNA, to enhance the accuracy of cancer diagnostics.

Quantification of DNA and RNA Using a Digital Dual CRISPR-Cas Assay. Digital assays such as digital PCR have already been widely applied for the absolute quantification of target molecules in individual partitions, facilitating single-molecule-level analysis.[62,63] Following this concept, we adapted the bulk reaction into a digital format using a microwell array chip (Figure S1A−C, Video S2). The operation of this microwell array chip can be divided into four steps: sample partitioning, oil sealing, incubation at 37 °C, and digital visualization. Briefly, synthetic templates of DNA and RNA were added to a 40 μL dual CRISPR-Cas mixture, thoroughly mixed, and then loaded into the chip. Sample partitioning was achieved by gravity, allowing the aqueous phase to distribute across the microwells, where synthetic templates of DNA and RNA were allocated according to a Poisson distribution. After the distribution of the reaction system, 100 μL of oil was added to seal the wells, and the chip was incubated at 37 °C for 30 min. To prevent the premature reaction of the dual CRISPR-Cas system before sample loading into the chip, all steps prior to oil sealing were conducted on ice. The results were then visualized using fluorescence microscopy, and the entire image processing workflow was completed using the built-in algorithms of NIS-Elements software (Figures S10 and S11).

The reaction time required for the simultaneous detection of Cas12a and Cas13a was assessed by using a microwell array chip. Once the templates with the CRISPR-Cas mixture were divided and isolated into individual microwells, the fluorescence signals in each microwell were continuously monitored and recorded at 1 min intervals. By diluting DNA and RNA templates to as low as 6×10^5 copies/μL, which means the mathematical expectation λ in Poisson distribution was 0.03, each microwell would be guaranteed to contain either 0 or 1 template molecule with over 99.9% probability. Under these conditions, both Cas12 and Cas13a showed digital detection patterns, confirming the capability of the dual CRISPR-Cas system to detect single-copy DNA and RNA templates. The fluorescence signal generated by Cas13a-cleaved RNA reporters reached a plateau within 5 min. In contrast, the Cas12a group required approximately 30 min to reach peak fluorescence, indicating that the trans-cleavage activity of Cas13a was much faster compared with that of Cas12a (Figure 3A,B, Video S1). Therefore, the on-chip reaction time was fixed at 30 min for subsequent experiments.

To evaluate the quantitative capabilities of the digital dual CRISPR-Cas assay, synthetic templates of DNA and RNA were prepared in serial dilutions ranging from 6×10^3 to 6×10^7 copies/μL for on-chip detection (Figure 3C). A good correlation between the number of positive microwells and the input concentrations of DNA and RNA was observed, maintaining linearity across 5 orders of magnitude with R^2 values exceeding 0.99 (Figure 3D). The limit of detection (LoD) of our digital dual CRISPR-Cas assay was calculated as few as 474.8 copies/μL of DNA and 551.8 copies/μL of RNA based on a background +3 × SD. These results confirmed the accuracy and

https://doi.org/10.1021/acsnano.4c13557
ACS Nano 2025, 19, 1271−1285

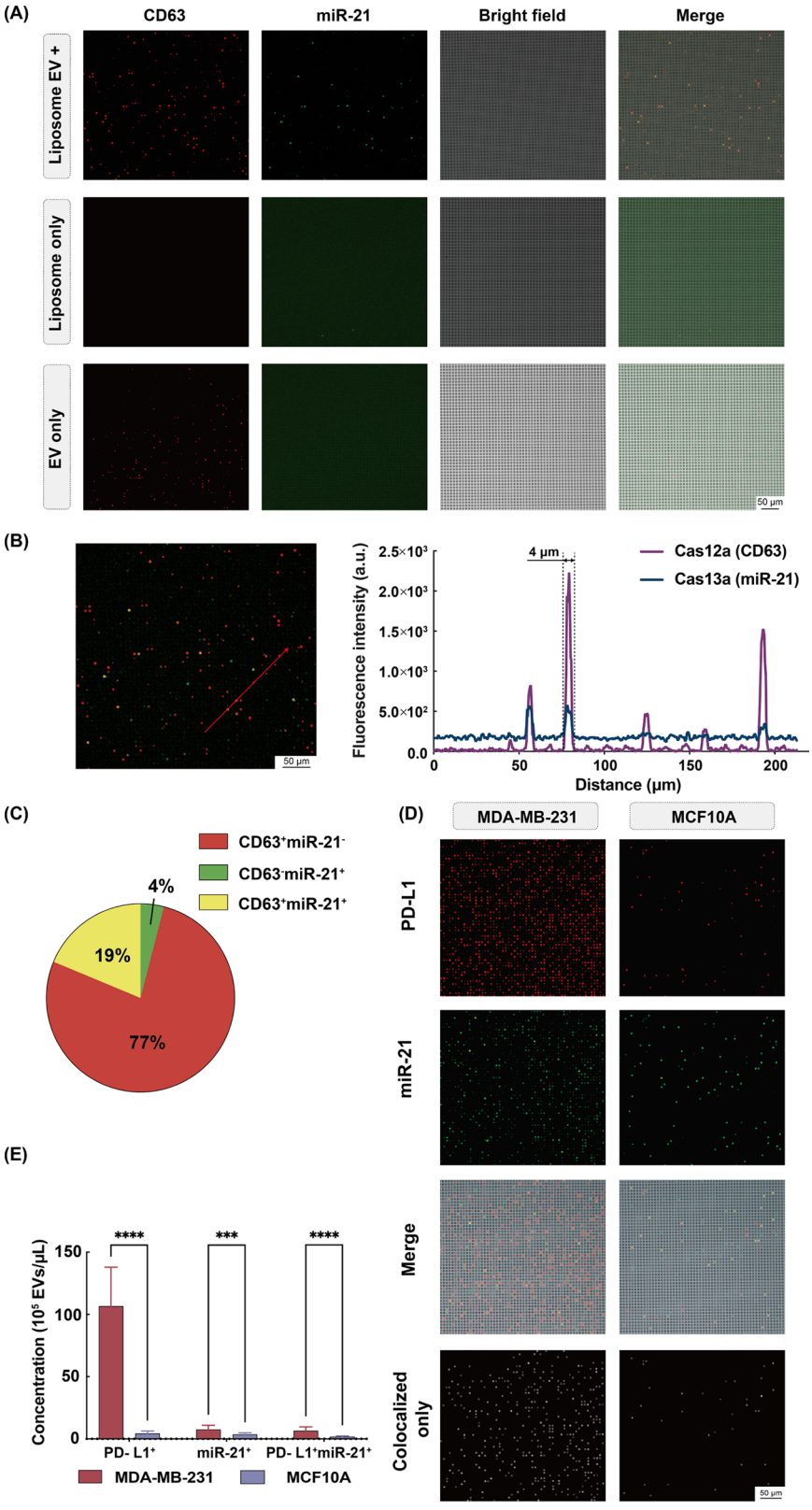


Figure 4. Measurement of EVs derived from the cell culture medium of breast cell lines. (A) Fluorescence microscopy images showing the simultaneous detection of the universal EV marker CD63 (red dots) and miR-21 (green dots). (B) Fluorescence microscopy images for the simultaneous detection of CD63 and the miR-21 in individual EVs from the culture medium of MDA-MB-231 cell and colocalization analysis of fluorescence pictures carried out by creating profiles of red and green color intensities along cross sections (shown by red arrows). (C) The corresponding calculated percentage of $CD63^{+}miR\text{-}21^{-}$, $CD63^{-}miR\text{-}21^{+}$, and $CD63^{+}miR\text{-}21^{+}$ EVs detected by the ddSEE system. (D) Representative images displayed the expression of PD-L1 and miR-21 in individual EVs derived from MDA-MB-231 and MCF10A cells. (E) The data presented the concentrations of $PD\text{-}L1^{+}$, $miR\text{-}21^{+}$, and $PD\text{-}L1^{+}miR\text{-}21^{+}$ EVs. A statistically significant difference was observed among these groups, as determined by the *t* test.

https://doi.org/10.1021/acsnano.4c13557
ACS Nano 2025, 19, 1271−1285

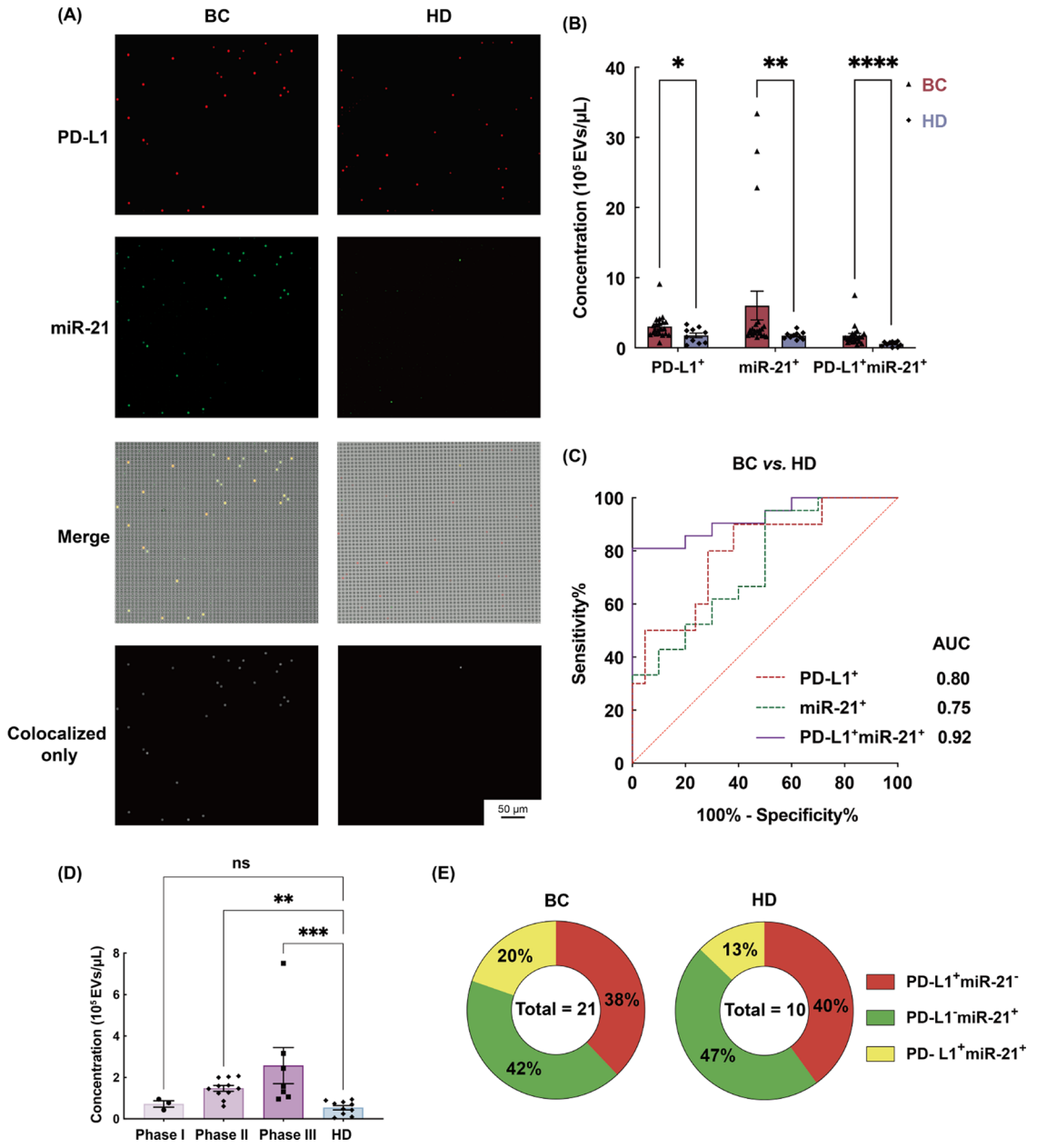


Figure 5. Application of the ddSEE system for breast cancer diagnosis. (A) Representative fluorescence images of PD-L1 and miR-21 in individual EVs from patients with breast cancer (BC) and healthy donors (HD). (B) Concentrations of PD-L1$^+$miR-21$^-$, PD-L1$^-$miR-21$^+$, and PD-L1$^+$miR-21$^+$ EVs measured in the clinical samples. (C) Comparison of the EV markers PD-L1, miR-21, and the colocalization of both markers through the receiving operator characteristic (ROC) curve analysis. AUC referred to the area under the ROC curve. (D) Concentration of PD-L1$^+$miR-21$^+$ EVs from patients with phase I, II, and III BC as well as HD. Statistically significant differences were determined using *t* test. (E) Averaged ratios of EVs subpopulations in patients with BC and HD.

consistency of the digital dual CRISPR-Cas assay for the quantitative detection of nucleic acids.

It can be noted that the detection limit of the Cas12a and Cas13a bulk assay was limited to 100 and 500 fM, respectively. By partitioning the bulk reaction (20 μL) into 188,000 microwells (50 fL) to perform a digital assay, the ultralocalized Cas12a and Cas13a assay significantly improved the detection limit over 100-fold (Figure 3G). Furthermore, continuous cleavage of the probes by Cas12a and Cas13a led to signal amplification, achieving average signal-to-noise ratios of 5.1 for Cas12a and 2.5 for Cas13a within microwells, respectively (Figure 3E,F). Compared to molecular beacon-based methods[14,64,65] that lack a signal amplification step, this digital dual CRISPR-Cas assay achieved higher signal-to-noise ratios for single-molecule detection.

Concurrent Detection of PD-L1 and miR-21 in EVs. To create a concurrent reaction environment conducive to single EV analysis, a liposome fusion strategy was utilized to realize the Cas13a-based detection of miR-21 in EVs, whereas an antibody-DNA conjugate was used for Cas12a-based surface protein detection in EVs. Conjugation with dibenzocyclooctyne-PEG4-*N*-hydroxysuccinimidyl ester (DBCO-PEG4-NHS) was used to label antibodies with the Cas12a activation sequence.[66] The conjugated DNA sequence in this study contained a target sequence flanked by two spacer arms, minimizing steric hindrance and facilitating binding of dsDNA to the Cas12a

https://doi.org/10.1021/acsnano.4c13557
ACS Nano 2025, 19, 1271−1285

protein (Figure S12). The protospacer adjacent motif (PAM) region of this DNA sequence was carefully designed to ensure that the Cas12a cleavage site was positioned distal to the antibodies (Figure S13). The DBCO-PEG4-NHS/antibody ratio was chosen to be within 20−30 (Figure S14A−C). The conjugation of the DNA oligo did not significantly affect the capacity of the secondary antibody to recognize the primary antibody (Figure S15). Furthermore, the specificity of Cas13a in the detection of miR-21 was validated. Our microwell-based Cas13a assay showed excellent specificity for the selective quantification of miR-21 from similarly sequenced miRNAs, such as miR-122 and miR-210 (Figure S16).

Next, the ddSEE system was used to simultaneously detect universal EV marker CD63 and potential tumor marker miR-21. Notably, CD63 and miR-21 were successfully detected in the EVs, whereas controls without EVs exhibited no fluorescence. Meanwhile, in the EV-only group as a control, the absence of liposomes resulted in the inability of Cas13a to be delivered for RNA detection within the EVs, leading to the absence of a detectable green RNA signal. This underscores the essential role of liposomes in mediating the delivery of Cas13a into EVs. These results validated the potential of our ddSEE system for the simultaneous and precise analysis of both surface protein and miRNA in EVs (Figure 4A). After a 30 min on-chip incubation, the coexistence of CD63 and miR-21 was evidenced by merging red and green fluorescence signals from the Cas12a-cleaved DNA probes and the Cas13a-cleaved RNA probes, respectively, showing a distinctive yellow fluorescence (Figure 4B). Correspondingly, $CD63^+miR\text{-}21^+$ EVs comprised 19% of the EV population, while $CD63^+miR\text{-}21^-$ EVs accounted for 77%. In contrast, only 4% of $CD63^-miR\text{-}21^+$ EVs were detected (Figure 4C). These findings are consistent with previous results obtained using flow cytometry.[67,68] Then, we performed serial dilutions of EVs, establishing a linear relationship between $CD63^+$ EVs concentrations and their dilution factors. The assay covered a dynamic range of 4 orders of magnitude and achieved a detection limit of 214 EVs with the lowest concentrations experimentally detected as 2×10^3 EVs/μL. (Figure S17).

Next, EVs derived from the culture medium of BC cell line MDA-MB-231 and normal mammary epithelial cell line MCF10A were assessed to evaluate the expression levels of PD-L1 and miR-21 in individual EVs. As shown in Figure 4D,E, PD-L1 and miR-21 concentrations were considerably higher in EVs from the MDA-MB-231 cells than those from the MCF10A cells, consistent with previous reports[57,69] and corroborate the findings from conventional flow cytometry and qPCR assays (Figure 2D,E). Collectively, these results underscored the differential expression of PD-L1 and miR-21 in EVs between cancerous and noncancerous cell lines.

Tests of Clinical Samples for Breast Cancer Diagnosis. To optimize EV isolation for clinical analysis, we first compared ultracentrifugation, anion exchange beads, and size-exclusion chromatography for isolating EVs from plasma. EV purity and concentration were assessed by staining with CD9 and CD63 surface protein markers, followed by analysis using nanoflow cytometry (Figure S18A). Ultracentrifugation achieved the highest purity (28%), outperforming anion exchange beads (17%) and size-exclusion chromatography columns from Izon (4.8%) and ECHO AIOTECH (4.4%) (Figure S18B). EV concentrations, determined after a 500-fold dilution, were highest with ultracentrifugation (2.25×10^9 particles/mL), followed by anion exchange beads (1.76×10^8 particles/mL), size-exclusion chromatography columns from Izon (1.83×10^8 particles/mL) and ECHO AIOTECH (5.17×10^8 particles/mL) (Figure S18C). Therefore, ultracentrifugation was selected as the preferred method for EV isolation in our study.

The capability of our ddSEE system for cancer diagnosis was validated by detecting EVs derived from the plasma samples of patients with BC (n = 21) and HD (n = 10). Detailed information about the patients and HD was provided in Tables S4 and S5. Because BC is uncommon in men, this study included only female patients and controls. Fluorescence imaging revealed the presence of PD-L1 and miR-21 in individual EVs from HD and patients with BC (Figure 5A, Figures S19 and S20). The concentrations of $PD\text{-}L1^+$, $miR\text{-}21^+$, and $PD\text{-}L1^+miR\text{-}21^+$ EVs were also measured (Figure 5B).

Although the statistical results showed that the amount of $PD\text{-}L1^+$ EVs or $miR\text{-}21^+$ EVs in the plasma from patients with BC was significantly greater than that from HD, the concurrent assessment of PD-L1 and miR-21 on single EVs improved the discrimination of patients with BC from HD, exceeding the use of PD-L1 or miR-21 as a single marker in EVs (Figure 5B,C). Additionally, by concurrently assessing PD-L1 and miR-21 in individual EVs, it was possible to distinguish patients with phase II and III BC from HD (Figure 5D). Meanwhile, a higher proportion of $PD\text{-}L1^+miR\text{-}21^+$ EVs was observed in patients with BC. The increased proportion of $PD\text{-}L1^+$ $miR\text{-}21^+$ EVs, independent of concentration (Figure 5E, Figure S21), were consistent with previous studies,[69,70] indicating the coexpression of PD-L1 and miR-21 within the same cells. This suggests a potential shared regulatory mechanism between PD-L1 and miR-21.[71,72] However, while the proportion of the $PD\text{-}L1^+miR\text{-}21^+$ subpopulation is valuable for diagnosis, it remains crucial to include concentration data for a more accurate assessment of the differences. Receiver operating characteristic (ROC) curve analysis confirmed the robustness of the dual-marker strategy for BC detection, with an area under the curve (AUC) value of 0.92, surpassing those of PD-L1 alone (AUC = 0.80) and miR-21 alone (AUC = 0.75) (Figure 5C). We determined the cutoff values for PD-L1 alone, miR-21 alone, and the concurrent assessment of dual markers PD-L1 and miR-21 on single EVs based on the Youden index. Each clinical sample was analyzed individually according to these cutoff values, allowing us to classify the samples as true positive, false positive, true negative, and false negative. The specificity and sensitivity for PD-L1 alone were 90 and 57%, respectively, while for miR-21 alone, the specificity and sensitivity were 50 and 95%. The concurrent assessment of dual markers PD-L1 and miR-21 on single EVs achieved a specificity of 100% and a sensitivity of 81%, further demonstrating the advantage of a dual-marker strategy (Figure S22). These results highlight the potential of our ddSEE system for the precise detection of BC, leveraging the analytical capabilities of single EV analysis to improve biomarker profiling for clinical diagnosis.

DISCUSSION

The increasing interest in utilizing EVs as biomarkers in liquid biopsies for cancer diagnosis, coupled with the challenge posed by the heterogeneity of blood EVs, has accelerated the development of methods for single-molecule EV analysis. In this study, ddSEE was developed for the simultaneous detection of protein and miRNA in individual EVs. This assay can reliably quantify as few as 474.8 copies/μL of DNA and 551.8 copies/μL of RNA. The lowest concentrations experimentally detected were 6×10^3 copies/μL for both DNA and RNA in gradient dilution experiments, while maintaining excellent linearity

https://doi.org/10.1021/acsnano.4c13557
ACS Nano 2025, 19, 1271−1285

across 5 orders of magnitude. By conversion of protein signals into DNA signals using antibody-DNA conjugates and employing EV-liposome fusion, the surface protein and inner miRNA of individual EVs can be simultaneously detected using the digital dual CRISPR-Cas system. The concurrent detection of PD-L1 and miR-21 achieved 92% accuracy in distinguishing 21 patients with BC from 10 HD.

Compared with the existing methods for single EV analysis (Figure S23), our ddSEE system offers three advantages. First, this method achieves high accuracy in quantifying EV subpopulation concentrations and using liposome fusion for miRNA detection[33−36] in EVs minimizes contamination from free-circulating miRNAs, improving quantification accuracy. Additionally, this method allows for the accurate detection of a wide range of particle sizes. Although the majority of EVs detected in the experiments are distributed within the 50−200 nm range, the 4-μm diameter and depth microwells enable the detection of all particles smaller than 4 μm by adjusting the input particle size. Second, this system is easy to operate, and using the CRISPR-Cas system for signal amplification enables illumination of microwells within 30 min under a fluorescence microscope. Third, our system enables the concurrent detection of both protein and miRNA within individual EVs. This ability to concurrently analyze multiple types of biomarkers improves the detection of EV subpopulations, effectively addressing the challenge of specificity in blood-derived EVs. As proteins often serve as the functional units responsible for specific biological activities and miRNAs encapsulated within EVs primarily play a role in regulating gene expression in target cells,[73] the multiplex detection of protein and miRNA allows for a more precise investigation of EV subpopulations from two broad perspectives. Given its precision, user-friendliness, and ability to analyze multiple markers simultaneously in individual EVs, the ddSEE system introduced in this study holds considerable promise for advancing EV research and its applications in disease diagnosis.

Although we have demonstrated the feasibility of the ddSEE system as a potential tool for cancer diagnosis and performed initial assessments in the context of breast cancer, further validation of our results is necessary through expanding clinical trials with a larger number of participants, particularly, focusing on patients with breast cancer in phase I.

At present, our system still relies on ultracentrifugation to purify EVs, which is not conducive to the subsequent fabrication of integrated detection devices. During the sample loading process, although 20 μL of the EV sample is used, less than 10 nL of sample actually enters the microwells for final counting, reducing the overall detection efficiency. In the future, we aim to adopt magnetic bead separation to circumvent the reliance on ultracentrifugation for EVs purification, making the method more suitable for small-volume sample detection. Additionally, the number of microwells was increased to further improve detection sensitivity. While ddSEE has achieved single-molecule detection and precise quantification of EV subpopulations, the accurate quantification of individual molecules within single EVs remains a significant challenge and will be a key focus of our future research. Despite the potential for further optimization, we firmly believe that our ddSEE system, with its capability to concurrently detect the surface protein and inner miRNA of individual EVs at the single-molecule level, significantly enhances our understanding of the heterogeneity of EVs at the single EV level and improves precise disease diagnosis in clinical settings.

METHODS/EXPERIMENTAL SECTION

Cell Culture. The MDA-MB-231 and MCF10A cell lines were obtained from the Xiehe Cell Resource Center. MDA-MB-231 cells were cultured in Dulbecco's modified Eagle's medium (DMEM, Sigma-Aldrich, Shanghai, China) supplemented with 10% (v/v) fetal bovine serum and 1% (v/v) penicillin-streptomycin solution. MCF10A cells were maintained in a specialized medium comprising DMEM/Ham's F-12 (11039-021, GIBCO, Shanghai, China), 10 μg/mL insulin (CC101, M&C GENE, Beijing, China), 0.1 μg/mL cholera toxin (CC104, M&C GENE), 0.5 μg/mL hydrocortisone (CC103, M&C GENE), 20 ng/mL EGF (CC102, M&C GENE), 15 mM HEPES (16050-130, GIBCO), and 5% horse serum (16050-130, GIBCO).

Clinical Samples. After the informed consent was obtained, 21 blood samples from patients with breast cancer and 10 blood samples from healthy donors were collected. Detailed information regarding the blood samples can be found in Tables S4 and S5. All procedures involving blood sample collection were approved by the Tsinghua University Science and Technology Ethics Committee (IRB Number: THU01-20240301). The blood samples were collected and centrifuged twice at 2000g for 30 min to isolate the cell-free plasma. The plasma was carefully collected and stored at −80 °C until further use.

EV Isolation. Upon reaching 70% confluence, the culture medium for both MDA-MB-231 and MCF10A cells was replaced with a medium containing 10% (v/v) exosome-depleted serum. The cells were then cultured for an additional 24 h. Subsequently, the supernatant was collected and subjected to sequential centrifugation at 3000g for 30 min and then at 10,000g for another 30 min to remove cell debris and apoptotic bodies. The supernatant was carefully aspirated and filtered through a 0.22-μm pore-size filter (SLGPR33RB, Sigma-Aldrich), followed by ultracentrifugation at 160,000g with 70 Ti rotor at 4 °C for 70 min. The resulting pellet was resuspended in 27 mL of phosphate-buffered saline (PBS; GIBCO) and centrifuged again at 160,000g at 4 °C for 70 min to further purify the sample by washing away the residual proteins. To isolate EVs from plasma samples, 100 μL of plasma was diluted to 1 mL with PBS and subjected to the same high-speed centrifugation protocol as described above. Then, the diluted plasma was ultracentrifuged using a TLA-55 rotor for 30 min to obtain the EV pellet. After the final ultracentrifugation step, the isolated EVs were resuspended in 40 μL of PBS supplemented with protease inhibitors (20123ES10, Yeasen, Shanghai, China) for subsequent analyses.

EV Characterization Using TEM. For TEM analysis, an aliquot containing 20 μL of the EV suspension was dropped onto a carbon-coated grid and incubated for 5 min. The grid was washed twice with distilled water to remove the residual salts from the EV solution. The samples were then stained with 2% uranyl acetate for 30 s, and excess staining solution was removed by using filter paper. The grid was then imaged using an electron microscope (FEI Tecnai Spirit TEM D1266, Thermo Fisher, Shanghai, China).

Nanoparticle Tracking Analysis. Briefly, the EV samples were diluted 1:50 in PBS and loaded into the chamber of the NTA system (NanoSight LM14, Malvern Instruments, U.K.) by using a 1 mL syringe. The system was set to automatically analyze the size distribution and particle concentration of the EVs by using NanoSight NTA Software (Malvern Instruments). To assess the efficiency of different concentrations of Triton X-100 on EV lysis, Triton X-100 was added to 50 μL of EV suspensions at final concentrations of 0, 0.001, 0.01, 0.1, and 1%. After gentle mixing and incubation for 30 s, the samples were diluted 1:50 in PBS to prepare the NTA.

Western Blotting Analysis. Cell and EV samples were lysed using radioimmunoprecipitation assay (RIPA) buffer and mixed with a loading buffer (20315ES20, Yeasen). The mixtures were denatured at 95 °C for 10 min and centrifuged at 12,000g for 10 min. The prepared samples were then loaded onto a 4−12% gradient sodium dodecyl sulfate polyacrylamide gel electrophoresis (SDS-PAGE) gel (36255ES10, Yeasen) for protein separation. The proteins were then transferred to a polyvinylidene fluoride (PVDF) membrane, which was blocked with 5% milk for 45 min. Next, the membrane was incubated overnight at 4 °C with primary antibodies against ALIX (12422-1-AP; Proteintech, Wuhan, China), CD9 (ab236630; Abcam, Shanghai,

https://doi.org/10.1021/acsnano.4c13557
ACS Nano 2025, 19, 1271−1285

China), and Grp94 (2104T; Cell Signaling Technology, Shanghai, China). After overnight incubation, the membrane was washed three times with TBST (FB23435-500, FeiMoBio, Beijing, China), followed by a 1 h incubation at 20−25 °C with secondary antibodies (BE0101-100 and BE0102-100, Easybio, Beijing, China). After secondary antibody incubation, the membrane was washed three times before applying the enhanced chemiluminescence reagent for imaging.

qPCR Analysis. Total miRNA was extracted from both cellular and EV samples using a miRNA extraction kit (19332ES50, Yeasen) following the manufacturer's protocol. Subsequently, the extracted miRNA was reverse-transcribed to cDNA using a first-strand cDNA synthesis kit (MR101, Vazyme, Nanjing, China) following the manufacturer's instructions. qPCR analyses were performed by using a miRNA Universal SYBR qPCR Master Mix (MR101-01, Vazyme) to quantify miRNA expression levels. The primer sequences used in the analyses are listed in Table S3. The expression of miRNAs was normalized to that of RNA snoU6 and quantified based on the $2^{-\Delta\Delta Ct}$ method. Specifically, to calculate the relative expression levels of miR-21 in cell and EV samples, the average miR-21 expression level in mammary epithelial MCF10A cells was first determined from three replicates and set as the reference value of 1. The miR-21 expression levels in breast cancer cells were then normalized to the MCF10A average to obtain the relative expression levels. Similarly, for the EV samples, the average miR-21 expression in MCF10A-derived EVs was used as the reference value.

Flow Cytometry Analysis. The cell suspensions were centrifuged at 700*g* for 5 min in PBS. The supernatant was discarded, and the cell pellet was resuspended in 100 μL of PBS. For antibody staining, anti-PD-L1 primary antibodies (329701, BioLegend, Beijing, China) were added to the suspension at a 1:100 dilution and incubated at 4 °C for 1 h. After primary antibody staining, the cells were washed three times with PBS. FITC-labeled antimouse secondary antibodies (33207ES60, Yeasen) were then added to the cells at a 1:500 dilution followed by incubation for 1 h at 4 °C. Finally, the cells were washed three times with PBS and resuspended in 200 μL of PBS for flow cytometry analysis.

For EV samples, streptavidin-labeled beads (65001, Thermo Fisher) functionalized with biotin-labeled antibodies against CD63 (353017, BioLegend) were used for EV capture. Given the murine source of the capture antibodies, a switch was made to allow rabbit-derived PD-L1 antibodies as the primary detection antibodies and PE-labeled antirabbit antibodies (ab7007, Abcam) as the secondary antibodies. Antigen detection on EV/antibody/bead complexes was performed using a staining protocol similar to that employed for cell samples. The complexes were then analyzed by using on-bead flow cytometry.

For nanoflow cytometry detection, the size distribution and particle concentration of EVs were measured (U30E, NanoFCM, Xiamen, China). The instrument was calibrated with 250 nm SiNPs beads for concentration and a Silica Nanosphere Cocktail (53, 73, 96, and 120 nm, S23M-SEV, NanoFCM) for the size distribution. Particles were recorded over a 1 min interval with samples diluted in PBS and analyzed under 1.0 kPa pressure. Data were processed using NanoFCM Software V2.0. Immunofluorescent staining was performed by using Alexa Fluor 488 Mouse Anti-Human CD9 (NHA009-A488-5T, NanoFCM) and Alexa Fluor 647 Mouse Anti-Human CD63 (NHA063-A647-5T, NanoFCM).

Antibody-DNA Conjugation. Initially, additives were removed from the antibody solutions by using a desalting column to prepare the conjugated antibodies. The antibodies were then activated with DBCO-PEG4-NHS (A102P-2, Click Chemistry Tools, Scottsdale, AZ) at room temperature for 30 min, and the reaction was quenched with 1:10 (v/v) Tris-HCl (pH 7.5). The unreacted DBCO-NHS ester was then removed *via* dialysis, and the efficiency of DBCO incorporation was measured. Subsequently, 200 μM azide-DNA (Sangon, Shanghai, China) solution was added to the antibody solution, and the mixture was thoroughly mixed *via* pipetting. After overnight incubation at 4 °C, the azide-DNA was conjugated to the antibody. Conjugation efficiency was verified by running 1 μg of the antibody-DNA conjugate on SDS-PAGE and staining it with a silver staining kit (P0017S, Beyotime, Shanghai, China). Ladder patterns appearing above the 50 kDa molecular weight bands indicate strong labeling. Free oligonucleotides were removed using 100 kDa ultrafiltration tubes (UFC5100, Sigma-Aldrich), and the final products were stored in 50% glycerol at −20 °C until further analysis.

Buffer Construction and Optimization for One-Pot Assay. The buffer screening for Cas12a and Cas13a assays was conducted using 20 μL reaction mixtures. For Cas12a, each mixture contained 100 nM Cas12a, 125 nM synthesized IB-gRNA, 1 μM Reporter TA, and 50 pM synthesized Cas12a template (IB), while Cas13a mixtures included 20 nM Cas13a, 10 nM synthesized miR-21-gRNA, 500 nM Reporter 5U, and 50 pM synthesized Cas13a template (miR-21). Buffers that were screened are outlined in Table S1, with nontarget controls (NTC) serving as baselines. These mixtures were then subjected to isothermal incubation at 37 °C in Applied Biosystems 7500, with fluorescence intensities measured at 1 min intervals at a 30 min time frame to assess buffer performance.

To refine the buffer composition, an initial reaction used a base formulation comprising 40 mM Tris-HCl (pH 8.5), 6 mM $MgCl_2$, and 20 mM KCl. The optimization process included testing different pH values (7.0, 7.5, 8.0, 8.5, 9.0, 9.5, 10.0), $MgCl_2$ concentrations (0, 5, 10, 15, 20, 25, 30 mM), KCl concentrations (0, 20, 40, 60, 80, 100, 120 mM), Triton X-100 concentrations (0, 0.001, 0.01, 0.1, 1%), as well as varying concentrations of PEG 20000, PEG 10000, PEG 6000, PEG 200 (0, 2.5, 5, 7.5, 10%), and PVA (0, 0.025, 0.05, 0.1, 0.2%). Additionally, adjustments were made to the gRNA to Cas12a/Cas13a ratio (2:1, 1:1, 1:2, 1:4, 1:8) and preincubation time (0, 15, 30 min).

Evaluation of EV-Liposome Fusion with FRET. A total of 50 μL of EVs solution with a concentration of 1×10^{10} EVs/mL were stained with 20 μM DiI (C1036, Beyotime) and 20 μM DiD (C1039, Beyotime) by incubating at 37 °C for 1 h. Unbound dyes were removed by washing three times using a 300 kDa ultrafiltration tube (OD300C34, Pall, Beijing, China) at 13,800*g* for 2 min per wash, concentrating the EVs to a final volume of approximately 50 μL. Liposome aliquots (1×) at a concentration of 1×10^{11} liposomes/mL were prepared according to the manufacturer's instructions and diluted in 50 μL PBS, mixed with the DiI- and DiD-labeled EVs. Liposome-EV fusion reactions were performed at 37 °C for 30 min. After that, fluorescent signals were excited with a 480 nm laser and emission spectra were recorded from 525 to 750 nm using an EnSpire multimode microplate reader (PerkinElmer, Shanghai, China).

ddSEE Workflow. *Antibody-DNA-Labeling.* EVs enriched from 100 μL of plasma were incubated with antibody-DNA conjugates at room temperature for 1 h. The EV-antibody-DNA complexes were washed six times with PBS in a 300 kDa ultrafiltration tube (OD300C34, Pall, Beijing, China) at 13,800*g* for 2 min per wash. This washing process was used to remove any unbound antibody-DNA conjugates. The complexes were then washed twice with 1× dual CRISPR-Cas buffer containing 1 U of RNase (10610ES03, Yeasen) to replace the PBS. Finally, the complexes were resuspended in 50 μL of 1× dual CRISPR-Cas buffer containing 1 U of RNase for subsequent analyses.

Cas13a-Liposome Preparation. Following a slightly modified version of the protocol described in a previous study,[74] liposome complexes were prepared using a Lipofectamine CRISPRMAX Cas9 Transfection Reagent (CMAX00001, Thermo Fisher). Complex A was constituted by combining 40 nM LbuCas13a, 5 nM miR-21-specific gRNA, 2 U RNase inhibitor, and 1 μM FAM-tagged quencher reporter in a 1× dual CRISPR-Cas buffer. Complex B was prepared by mixing the transfection reagent with 1× dual CRISPR-Cas buffer. The two complexes were mixed gently and incubated at room temperature for 15 min.

On-Chip Reaction. The microwell array chips used in this study were provided by Iomics (Beijing, China). Initially, 10 μL of EV-antibody-DNA complexes, 10 μL of a Cas12a mixture, and 20 μL of a Cas13a-liposome were first prepared separately. The above solutions were then mixed and loaded into the chip, followed by a 1 min incubation on ice to ensure the liquid settled into the microwells. The EV-liposome fusion likely occurs immediately upon mixing because the fusion process typically occurs on a millisecond time scale. The chip was then sealed with 100 μL of oil and incubated at 37 °C for 30 min. Subsequently, the chip was imaged at 40× magnification with an inverted fluorescence

https://doi.org/10.1021/acsnano.4c13557
ACS Nano 2025, 19, 1271−1285

microscope (Nikon Ti2, Shanghai, China) equipped with a CMOS sensor (Nikon DS-Ri2), capturing both bright field and fluorescence images.

Image Processing and Data Analysis. Digital quantification of the bright field, FAM (green dots), and ROX (red dots) channel images and signal-to-background ratio (SBR) calculations were conducted using NIS-Elements software for fluorescence intensity analysis. All calculations were based on pixel values from the original images. For image presentation, contrast adjustments were uniformly applied to each point within the same batch and image, ensuring a clear visualization for readers without affecting the experimental results. For the specific analysis process, please refer to the "Data analysis process with Poisson distribution" in the Supporting Information.

Statistical Analysis. The data and figures were prepared using GraphPad Prism version 9.0 software (GraphPad Software, Inc., San Diego, CA). Statistical analyses were conducted using the Mann−Whitney U test, unpaired *t* test, and two-way analysis of variance (ANOVA) with multiple comparison tests. Differences with *p*-values <0.05 were considered statistically significant. Statistical significance is denoted as follows: (*) $0.01 < p < 0.05$, (**) $0.001 < p < 0.01$, (***) $0.0001 < p < 0.001$, and (****) $p < 0.0001$.

ASSOCIATED CONTENT

Supporting Information

The Supporting Information is available free of charge at https://pubs.acs.org/doi/10.1021/acsnano.4c13557.

Optimization of buffer components, optimization of gRNA-to-Cas protein ratio and preincubation time, optimization and assessment of antibody-DNA conjugation process, verification of the specificity of the Cas13a assay, EV gradient dilution experiment, end point fluorescence images of the ddSEE system for detecting clinical samples, image processing procedure, and data analysis process with Poisson distribution (Supporting text) (Figures S1−S23) (Tables S1−S5) (PDF)

Real-time fluorescence monitoring of digital dual CRISPR-Cas assay (Video S1) (MP4)

Main workflow of the ddSEE system with the microwell array chip (Video S2) (MP4)

AUTHOR INFORMATION

Corresponding Authors

Jing Cheng − *School of Biomedical Engineering, Tsinghua University, Beijing 100084, China; National Engineering Research Center for Beijing Biochip Technology, Beijing 102200, China*; Email: jcheng@tsinghua.edu.cn

Youchun Xu − *School of Biomedical Engineering, Tsinghua University, Beijing 100084, China; National Engineering Research Center for Beijing Biochip Technology, Beijing 102200, China*; orcid.org/0000-0003-4926-8211; Email: xyc2012@tsinghua.edu.cn

Authors

Xun Xu − *School of Biomedical Engineering, Tsinghua University, Beijing 100084, China*

Yuanyue Zhang − *School of Biomedical Engineering, Tsinghua University, Beijing 100084, China*

Jiajia Liu − *School of Biomedical Engineering, Tsinghua University, Beijing 100084, China; CapitalBio Technology, Beijing 101111, China*

Shujin Wei − *School of Biomedical Engineering, Tsinghua University, Beijing 100084, China*

Nan Li − *School of Biomedical Engineering, Tsinghua University, Beijing 100084, China; State Key Laboratory of Transducer Technology, Aerospace Information Research Institute, Chinese Academy of Sciences, Beijing 100190, China*

Xintong Yao − *School of Biomedical Engineering, Tsinghua University, Beijing 100084, China*

Muxue Wang − *School of Biomedical Engineering, Tsinghua University, Beijing 100084, China*

Xiaohan Su − *School of Biomedical Engineering, Tsinghua University, Beijing 100084, China*

Gaoshan Jing − *Institute of Microelectronics of the Chinese Academy of Sciences, Beijing 100029, China*

Junquan Xu − *Iomics Biosciences, Beijing 101318, China*

Yan Liu − *Iomics Biosciences, Beijing 101318, China*

Ying Lu − *School of Biomedical Engineering, Tsinghua University, Beijing 100084, China; National Engineering Research Center for Beijing Biochip Technology, Beijing 102200, China*

Complete contact information is available at: https://pubs.acs.org/10.1021/acsnano.4c13557

Author Contributions

[▽]X.X. and Y.Z. contributed equally to this work.

Notes

The authors declare no competing financial interest.

ACKNOWLEDGMENTS

This study was supported by the National Natural Science Foundation of China (32201246, 22074078), Beijing Nova Program 2020 and Beijing Lab Foundation.

REFERENCES

(1) Kalluri, R.; LeBleu, V. S. The Biology, Function, and Biomedical Applications of Exosomes. *Science* **2020**, *367*, No. eaau6977.

(2) Chevillet, J. R.; Kang, Q.; Ruf, I. K.; Briggs, H. A.; Vojtech, L. N.; Hughes, S. M.; Cheng, H. H.; Arroyo, J. D.; Meredith, E. K.; Gallichotte, E. N.; Pogosova-Agadjanyan, E. L.; Morrissey, C.; Stirewalt, D. L.; Hladik, F.; Yu, E. Y.; Higano, C. S.; Tewari, M. Quantitative and Stoichiometric Analysis of the microRNA Content of Exosomes. *Proc. Natl. Acad. Sci. U.S.A.* **2014**, *111*, 14888−14893.

(3) Willms, E.; Cabañas, C.; Mäger, I.; Wood, M. J. A.; Vader, P. Extracellular Vesicle Heterogeneity: Subpopulations, Isolation Techniques, and Diverse Functions in Cancer Progression. *Front. Immunol.* **2018**, *9*, 738.

(4) Lässer, C.; Jang, S. C.; Lötvall, J. Subpopulations of Extracellular Vesicles and their Therapeutic Potential. *Mol. Aspects Med.* **2018**, *60*, 1−14.

(5) Ouyang, T.; Liu, Z.; Han, Z.; Ge, Q. MicroRNA Detection Specificity: Recent Advances and Future Perspective. *Anal. Chem.* **2019**, *91*, 3179−3186.

(6) Shao, H.; Im, H.; Castro, C. M.; Breakefield, X.; Weissleder, R.; Lee, H. New Technologies for Analysis of Extracellular Vesicles. *Chem. Rev.* **2018**, *118*, 1917−1950.

(7) Ferguson, S.; Yang, K. S.; Weissleder, R. Single Extracellular Vesicle Analysis for Early Cancer Detection. *Trends Mol. Med.* **2022**, *28*, 681−692.

(8) Zhang, J.; Wu, J.; Wang, G.; He, L.; Zheng, Z.; Wu, M.; Zhang, Y. Extracellular Vesicles: Techniques and Biomedical Applications Related to Single Vesicle Analysis. *ACS Nano* **2023**, *17*, 17668−17698.

(9) Ko, J.; Wang, Y.; Carlson, J. C. T.; Marquard, A.; Gungabeesoon, J.; Charest, A.; Weitz, D.; Pittet, M. J.; Weissleder, R. Single Extracellular Vesicle Protein Analysis Using Immuno-Droplet Digital Polymerase Chain Reaction Amplification. *Adv. Biosyst.* **2020**, *4* (12), No. 1900307.

(10) Ko, J.; Wang, Y.; Sheng, K.; Weitz, D. A.; Weissleder, R. Sequencing-Based Protein Analysis of Single Extracellular Vesicles. *ACS Nano* **2021**, *15*, 5631−5638.

(11) Lee, K.; Fraser, K.; Ghaddar, B.; Yang, K.; Kim, E.; Balaj, L.; Chiocca, E. A.; Breakefield, X. O.; Lee, H.; Weissleder, R. Multiplexed Profiling of Single Extracellular Vesicles. *ACS Nano* **2018**, *12*, 494−503.
(12) Reynolds, D. E.; Pan, M.; Yang, J.; Galanis, G.; Roh, Y. H.; Morales, R. T. T.; Kumar, S. S.; Heo, S. J.; Xu, X.; Guo, W.; Ko, J. Double Digital Assay for Single Extracellular Vesicle and Single Molecule Detection. *Adv. Sci.* **2023**, *10*, No. 2303619.
(13) Wei, Z.; Batagov, A. O.; Schinelli, S.; Wang, J.; Wang, Y.; El Fatimy, R.; Rabinovsky, R.; Balaj, L.; Chen, C. C.; Hochberg, F.; Carter, B.; Breakefield, X. O.; Krichevsky, A. M. Coding and Noncoding Landscape of Extracellular RNA Released by Human Glioma Stem Cells. *Nat. Commun.* **2017**, *8*, No. 1145.
(14) Zhou, J.; Wu, Z.; Hu, J.; Yang, D.; Chen, X.; Wang, Q.; Liu, J.; Dou, M.; Peng, W.; Wu, Y.; Wang, W.; Xie, C.; Wang, M.; Song, Y.; Zeng, H.; Bai, C. High-Throughput Single-EV Liquid Biopsy: Rapid, Simultaneous, and Multiplexed Detection of Nucleic Acids, Proteins, and their Combinations. *Sci. Adv.* **2020**, *6*, No. eabc1204.
(15) He, D.; Wang, H.; Ho, S.; Chan, H.; Hai, L.; He, X.; Wang, K.; Li, H. Total Internal Reflection-Based Single-Vesicle *in situ* Quantitative and Stoichiometric Analysis of Tumor-Derived Exosomal microRNAs for Diagnosis and Treatment Monitoring. *Theranostics* **2019**, *9*, 4494−4507.
(16) Tsourkas, A. Hybridization Kinetics and Thermodynamics of Molecular Beacons. *Nucleic Acids Res.* **2003**, *31*, 1319−1330.
(17) Hu, J.; Kwak, K. J.; Shi, J.; Yu, B.; Sheng, Y.; Lee, L. J. Overhang Molecular Beacons Encapsulated in Tethered Cationic Lipoplex Nanoparticles for Detection of Single-Point Mutation in Extracellular Vesicle-Associated RNAs. *Biomaterials* **2018**, *183*, 20−29.
(18) Gootenberg, J. S.; Abudayyeh, O. O.; Lee, J. W.; Essletzbichler, P.; Dy, A. J.; Joung, J.; Verdine, V.; Donghia, N.; Daringer, N. M.; Freije, C. A.; Myhrvold, C.; Bhattacharyya, R. P.; Livny, J.; Regev, A.; Koonin, E. V.; Hung, D. T.; Sabeti, P. C.; Collins, J. J.; Zhang, F. Nucleic Acid Detection with CRISPR-Cas13a/C2c2. *Science* **2017**, *356*, 438−442.
(19) Kaminski, M. M.; Abudayyeh, O. O.; Gootenberg, J. S.; Zhang, F.; Collins, J. J. CRISPR-Based Diagnostics. *Nat. Biomed. Eng.* **2021**, *5*, 643−656.
(20) Chen, J. S.; Ma, E.; Harrington, L. B.; Da, C. M.; Tian, X.; Palefsky, J. M.; Doudna, J. A. CRISPR-Cas12a Target Binding Unleashes Indiscriminate Single-Stranded DNase Activity. *Science* **2018**, *360*, 436−439.
(21) Zhao, Q.; Pan, Y.; Luan, X.; Gao, Y.; Zhao, X.; Liu, Y.; Wang, Y.; Song, Y. Nano-Immunosorbent Assay Based on Cas12a/crRNA for Ultra-Sensitive Protein Detection. *Biosens. Bioelectron.* **2021**, *190*, No. 113450.
(22) Yin, W.; Li, L.; Yang, Y.; Yang, Y.; Liang, R.; Ma, L.; Dai, J.; Mao, G.; Ma, Y. Ultra-Sensitive Detection of the SARS-CoV-2 Nucleocapsid Protein *via* a Clustered Regularly Interspaced Short Palindromic Repeat/Cas12a-Mediated Immunoassay. *ACS Sens.* **2024**, *9*, 3150−3157.
(23) Qi, L.; Liu, J.; Liu, S.; Liu, Y.; Xiao, Y.; Zhang, Z.; Zhou, W.; Jiang, Y.; Fang, X. Ultrasensitive Point-of-Care Detection of Protein Markers Using an Aptamer-CRISPR/Cas12a-Regulated Liquid Crystal Sensor (ALICS). *Anal. Chem.* **2024**, *96*, 866−875.
(24) Kang, Y.; Su, G.; Yu, Y.; Cao, J.; Wang, J.; Yan, B. CRISPR-Cas12a-Based Aptasensor for On-Site and Highly Sensitive Detection of Microcystin-LR in Freshwater. *Environ. Sci. Technol.* **2022**, *56*, 4101−4110.
(25) Yue, H.; Shu, B.; Tian, T.; Xiong, E.; Huang, M.; Zhu, D.; Sun, J.; Liu, Q.; Wang, S.; Li, Y.; Zhou, X. Droplet Cas12a Assay Enables DNA Quantification from Unamplified Samples at the Single-Molecule Level. *Nano Lett.* **2021**, *21*, 4643−4653.
(26) Tian, T.; Shu, B.; Jiang, Y.; Ye, M.; Liu, L.; Guo, Z.; Han, Z.; Wang, Z.; Zhou, X. An Ultralocalized Cas13a Assay Enables Universal and Nucleic Acid Amplification-Free Single-Molecule RNA Diagnostics. *ACS Nano* **2021**, *15*, 1167−1178.
(27) Wang, D.; Wang, X.; Ye, F.; Zou, J.; Qu, J.; Jiang, X. An Integrated Amplification-Free Digital CRISPR/Cas-Assisted Assay for Single Molecule Detection of RNA. *ACS Nano* **2023**, *17*, 7250−7256.
(28) Zhou, S.; Hu, T.; Han, G.; Wu, Y.; Hua, X.; Su, J.; Jin, W.; Mou, Y.; Mou, X.; Li, Q.; Liu, S. Accurate Cancer Diagnosis and Stage Monitoring Enabled by Comprehensive Profiling of Different Types of Exosomal Biomarkers: Surface Proteins and miRNAs. *Small* **2020**, *16*, No. 2004492.
(29) Rettig, J. R.; Folch, A. Large-Scale Single-Cell Trapping and Imaging Using Microwell Arrays. *Anal. Chem.* **2005**, *77*, 5628−5634.
(30) Rissin, D. M.; Kan, C. W.; Campbell, T. G.; Howes, S. C.; Fournier, D. R.; Song, L.; Piech, T.; Patel, P. P.; Chang, L.; Rivnak, A. J.; Ferrell, E. P.; Randall, J. D.; Provuncher, G. K.; Walt, D. R.; Duffy, D. C. Single-Molecule Enzyme-Linked Immunosorbent Assay Detects Serum Proteins at Subfemtomolar Concentrations. *Nat. Biotechnol.* **2010**, *28*, 595−599.
(31) Wilson, D. H.; Rissin, D. M.; Kan, C. W.; Fournier, D. R.; Piech, T.; Campbell, T. G.; Meyer, R. E.; Fishburn, M. W.; Cabrera, C.; Patel, P. P.; Frew, E.; Chen, Y.; Chang, L.; Ferrell, E. P.; von Einem, V.; McGuigan, W.; Reinhardt, M.; Sayer, H.; Vielsack, C.; Duffy, D. C. The Simoa HD-1 Analyzer: A Novel Fully Automated Digital Immunoassay Analyzer with Single-Molecule Sensitivity and Multiplexing. *SLAS Technol.* **2016**, *21*, 533−547.
(32) Ansaryan, S.; Liu, Y.; Li, X.; Economou, A. M.; Eberhardt, C. S.; Jandus, C.; Altug, H. High-Throughput Spatiotemporal Monitoring of Single-Cell Secretions *via* Plasmonic Microwell Arrays. *Nat. Biomed. Eng.* **2023**, *7*, 943−958.
(33) Hong, J. S.; Son, T.; Castro, C. M.; Im, H. CRISPR/Cas13a-Based microRNA Detection in Tumor-Derived Extracellular Vesicles. *Adv. Sci.* **2023**, *10*, No. 2301766.
(34) Gao, X.; Li, S.; Ding, F.; Fan, H.; Shi, L.; Zhu, L.; Li, J.; Feng, J.; Zhu, X.; Zhang, C. Rapid Detection of Exosomal microRNAs Using Virus-Mimicking Fusogenic Vesicles. *Angew. Chem., Int. Ed.* **2019**, *58*, 8719−8723.
(35) Ning, B.; Huang, Z.; Youngquist, B. M.; Scott, J. W.; Niu, A.; Bojanowski, C. M.; Zwezdaryk, K. J.; Saba, N. S.; Fan, J.; Yin, X.; Cao, J.; Lyon, C. J.; Li, C.; Roy, C. J.; Hu, T. Y. Liposome-Mediated Detection of SARS-CoV-2 RNA-Positive Extracellular Vesicles in Plasma. *Nat. Nanotechnol.* **2021**, *16*, 1039−1044.
(36) Cui, L.; Peng, R.; Zeng, C.; Zhang, J.; Lu, Y.; Zhu, L.; Huang, M.; Tian, Q.; Song, Y.; Yang, C. A General Strategy for Detection of Tumor-Derived Extracellular Vesicle microRNAs Using Aptamer-Mediated Vesicle Fusion. *Nano Today* **2022**, *46*, No. 101599.
(37) Park, J. S.; Akarapipad, P.; Chen, F.; Shao, F.; Mostafa, H.; Hsieh, K.; Wang, T. Digitized Kinetic Analysis Enhances Genotyping Capacity of CRISPR-Based Biosensing. *ACS Nano* **2024**, *18*, 18058−18070.
(38) Nguyen, L. T.; Smith, B. M.; Jain, P. K. Enhancement of Trans-Cleavage Activity of Cas12a with Engineered crRNA Enables Amplified Nucleic Acid Detection. *Nat. Commun.* **2020**, *11*, No. 4906.
(39) Nalefski, E. A.; Patel, N.; Leung, P.; Islam, Z.; Kooistra, R. M.; Parikh, I.; Marion, E.; Knott, G. J.; Doudna, J. A.; Le Ny, A. M.; Madan, D. Kinetic Analysis of Cas12a and Cas13a RNA-Guided Nucleases for Development of Improved CRISPR-Based Diagnostics. *iScience* **2021**, *24*, No. 102996.
(40) East-Seletsky, A.; O Connell, M. R.; Knight, S. C.; Burstein, D.; Cate, J. H. D.; Tjian, R.; Doudna, J. A. Two Distinct RNase Activities of CRISPR-C2c2 Enable Guide-RNA Processing and RNA Detection. *Nature* **2016**, *538*, 270−273.
(41) Yang, Y.; Sun, L.; Zhao, J.; Jiao, Y.; Han, T.; Zhou, X. Improving Trans-Cleavage Activity of CRISPR-Cas13a Using Engineered crRNA with a Uridinylate-Rich 5′-Overhang. *Biosens. Bioelectron.* **2024**, *255*, No. 116239.
(42) Shinoda, H.; Iida, T.; Makino, A.; Yoshimura, M.; Ishikawa, J.; Ando, J.; Murai, K.; Sugiyama, K.; Muramoto, Y.; Nakano, M.; Kiga, K.; Cui, L.; Nureki, O.; Takeuchi, H.; Noda, T.; Nishimasu, H.; Watanabe, R. Automated Amplification-Free Digital RNA Detection Platform for Rapid and Sensitive SARS-CoV-2 Diagnosis. *Commun. Biol.* **2022**, *5*, No. 473.
(43) Shao, F.; Park, J. S.; Zhao, G.; Hsieh, K.; Wang, T. Elucidating the Role of CRISPR/Cas in Single-Step Isothermal Nucleic Acid Amplification Testing Assays. *Anal. Chem.* **2023**, *95*, 3873−3882.

https://doi.org/10.1021/acsnano.4c13557
ACS Nano 2025, 19, 1271−1285

(44) Tian, T.; Qiu, Z.; Jiang, Y.; Zhu, D.; Zhou, X. Exploiting the Orthogonal CRISPR-Cas12a/Cas13a Trans-Cleavage for Dual-Gene Virus Detection Using a Handheld Device. *Biosens. Bioelectron.* **2022**, *196*, No. 113701.
(45) Feng, W.; Zhang, H.; Le, X. C. Signal Amplification by the Trans-Cleavage Activity of CRISPR-Cas Systems: Kinetics and Performance. *Anal. Chem.* **2023**, *95*, 206−217.
(46) Swarts, D. C.; van der Oost, J.; Jinek, M. Structural Basis for Guide RNA Processing and Seed-Dependent DNA Targeting by CRISPR-Cas12a. *Mol. Cell* **2017**, *66*, 221−233.
(47) Zhang, C.; Konermann, S.; Brideau, N. J.; Lotfy, P.; Wu, X.; Novick, S. J.; Strutzenberg, T.; Griffin, P. R.; Hsu, P. D.; Lyumkis, D. Structural Basis for the RNA-Guided Ribonuclease Activity of CRISPR-Cas13D. *Cell* **2018**, *175*, 212−223.
(48) Lv, H.; Wang, J.; Zhang, J.; Chen, Y.; Yin, L.; Jin, D.; Gu, D.; Zhao, H.; Xu, Y.; Wang, J. Definition of CRISPR Cas12a Trans-Cleavage Units to Facilitate CRISPR Diagnostics. *Front. Microbiol.* **2021**, *12*, No. 766464.
(49) Deng, F.; Li, Y.; Li, B.; Goldys, E. M. Increasing Trans-Cleavage Catalytic Efficiency of Cas12a and Cas13a with Chemical Enhancers: Application to Amplified Nucleic Acid Detection. *Sens. Actuators, B* **2022**, *373*, No. 132767.
(50) Hsieh, K.; Zhao, G.; Wang, T. H. Applying Biosensor Development Concepts to Improve Preamplification-Free CRISPR/Cas12a-Dx. *Analyst* **2020**, *145*, 4880−4888.
(51) Osteikoetxea, X.; Sodar, B.; Nemeth, A.; Szabo-Taylor, K.; Paloczi, K.; Vukman, K. V.; Tamasi, V.; Balogh, A.; Kittel, A.; Pallinger, E.; Buzas, E. I. Differential Detergent Sensitivity of Extracellular Vesicle Subpopulations. *Org. Biomol. Chem.* **2015**, *13*, 9775−9782.
(52) Habimana, J. D. D.; Mukama, O.; Chen, G.; Chen, M.; Amissah, O. B.; Wang, L.; Liu, Y.; Sun, Y.; Li, A. L.; Deng, S.; Huang, J.; Yan, X.; Rutaganda, T.; Mutangana, D.; Wu, L.; Huang, R.; Li, Z. Harnessing Enhanced CRISPR/Cas12a Trans-Cleavage Activity with Extended Reporters and Reductants for Early Diagnosis of Helicobacter Pylori, the Causative Agent of Peptic Ulcers and Stomach Cancer. *Biosens. Bioelectron.* **2023**, *222*, No. 114939.
(53) Yang, G.; Liu, Y.; Hui, Y.; Chen, D.; Weitz, D. A.; Zhao, C. X. Implications of Quenching to Dequenching Switch in Quantitative Cell Uptake and Biodistribution of Dye Labeled Nanoparticles. *Angew. Chem., Int. Ed.* **2021**, *60*, 15426−15435.
(54) Welsh, J. A.; Goberdhan, D. C. I.; O'Driscoll, L.; Buzas, E. I.; Blenkiron, C.; Bussolati, B.; Cai, H.; Di Vizio, D.; Driedonks, T. A. P.; Erdbrügger, U.; Falcon Perez, J. M.; Fu, Q. L.; Hill, A. F.; Lenassi, M.; Lim, S. K.; Mahoney, M. G.; Mohanty, S.; Möller, A.; Nieuwland, R.; Ochiya, T.; Sahoo, S.; et al. Minimal Information for Studies of Extracellular Vesicles (MISEV2023): From Basic to Advanced Approaches. *J. Extracell. Vesicles* **2024**, *13*, No. e12404.
(55) Daassi, D.; Mahoney, K. M.; Freeman, G. J. The Importance of Exosomal PDL1 in Tumour Immune Evasion. *Nat. Rev. Immunol.* **2020**, *20*, 209−215.
(56) Chen, G.; Huang, A. C.; Zhang, W.; Zhang, G.; Wu, M.; Xu, W.; Yu, Z.; Yang, J.; Wang, B.; Sun, H.; Xia, H.; Man, Q.; Zhong, W.; Antelo, L. F.; Wu, B.; Xiong, X.; Liu, X.; Guan, L.; Li, T.; Liu, S.; et al. Exosomal PD-L1 Contributes to Immunosuppression and is Associated with Anti-PD-1 Response. *Nature* **2018**, *560*, 382−386.
(57) Hannafon, B. N.; Trigoso, Y. D.; Calloway, C. L.; Zhao, Y. D.; Lum, D. H.; Welm, A. L.; Zhao, Z. J.; Blick, K. E.; Dooley, W. C.; Ding, W. Q. Plasma Exosome microRNAs are Indicative of Breast Cancer. *Breast Cancer Res.* **2016**, *18*, No. 90.
(58) Bautista-Sánchez, D.; Arriaga-Canon, C.; Pedroza-Torres, A.; De La Rosa-Velázquez, I. A.; González-Barrios, R.; Contreras-Espinosa, L.; Montiel-Manríquez, R.; Castro-Hernández, C.; Fragoso-Ontiveros, V.; Álvarez-Gómez, R. M.; Herrera, L. A. The Promising Role of miR-21 as a Cancer Biomarker and its Importance in RNA-Based Therapeutics. *Mol. Ther. Nucleic Acids* **2020**, *20*, 409−420.
(59) Wu, L.; Qu, X. Cancer Biomarker Detection: Recent Achievements and Challenges. *Chem. Soc. Rev.* **2015**, *44*, 2963−2997.
(60) Chang, S. T.; Zahn, J. M.; Horecka, J.; Kunz, P. L.; Ford, J. M.; Fisher, G. A.; Le, Q. T.; Chang, D. T.; Ji, H.; Koong, A. C. Identification of a Biomarker Panel Using a Multiplex Proximity Ligation Assay Improves Accuracy of Pancreatic Cancer Diagnosis. *J. Transl. Med.* **2009**, *7*, No. 105.
(61) Vinik, Y.; Ortega, F. G.; Mills, G. B.; Lu, Y.; Jurkowicz, M.; Halperin, S.; Aharoni, M.; Gutman, M.; Lev, S. Proteomic Analysis of Circulating Extracellular Vesicles Identifies Potential Markers of Breast Cancer Progression, Recurrence, and Response. *Sci. Adv.* **2020**, *6*, No. eaba5714.
(62) Morales, R. T.; Ko, J. Future of Digital Assays to Resolve Clinical Heterogeneity of Single Extracellular Vesicles. *ACS Nano* **2022**, *16*, 11619−11645.
(63) Hindson, C. M.; Chevillet, J. R.; Briggs, H. A.; Gallichotte, E. N.; Ruf, I. K.; Hindson, B. J.; Vessella, R. L.; Tewari, M. Absolute Quantification by Droplet Digital PCR Versus Analog Real-Time PCR. *Nat. Methods* **2013**, *10*, 1003−1005.
(64) Yang, Y.; Kannisto, E.; Yu, G.; Reid, M. E.; Patnaik, S. K.; Wu, Y. An Immuno-Biochip Selectively Captures Tumor-Derived Exosomes and Detects Exosomal RNAs for Cancer Diagnosis. *ACS Appl. Mater. Interfaces* **2018**, *10*, 43375−43386.
(65) Wu, Y.; Kwak, K. J.; Agarwal, K.; Marras, A.; Wang, C.; Mao, Y.; Huang, X.; Ma, J.; Yu, B.; Lee, R.; Vachani, A.; Marcucci, G.; Byrd, J. C.; Muthusamy, N.; Otterson, G.; Huang, K.; Castro, C. E.; Paulaitis, M.; Nana-Sinkam, S. P.; Lee, L. J. Detection of Extracellular RNAs in Cancer and Viral Infection *via* Tethered Cationic Lipoplex Nanoparticles Containing Molecular Beacons. *Anal. Chem.* **2013**, *85*, 11265−11274.
(66) Gong, H.; Holcomb, I.; Ooi, A.; Wang, X.; Majonis, D.; Unger, M. A.; Ramakrishnan, R. Simple Method to Prepare Oligonucleotide-Conjugated Antibodies and its Application in Multiplex Protein Detection in Single Cells. *Bioconjugate Chem.* **2016**, *27*, 217−225.
(67) Yang, H. C.; Rhee, W. J. Single Step *in situ* Detection of Surface Protein and microRNA in Clustered Extracellular Vesicles Using Flow Cytometry. *J. Clin. Med.* **2021**, *10*, 319.
(68) Li, Z.; Guo, K.; Gao, Z.; Chen, J.; Ye, Z.; Cao, M.; Wang, S. E.; Yin, Y.; Zhong, W. Colocalization of Protein and microRNA Markers Reveals Unique Extracellular Vesicle Subpopulations for Early Cancer Detection. *Sci. Adv.* **2024**, *10*, No. eadh8689.
(69) Zhang, J.; Guan, M.; Lv, M.; Liu, Y.; Zhang, H.; Zhang, Z.; Zhang, K. Localized Imaging of Programmed Death-Ligand 1 On Individual Tumor-Derived Extracellular Vesicles for Prediction of Immunotherapy Response. *ACS Nano* **2023**, *17*, 20120−20134.
(70) Lee, J. Y.; Lee, S.; Lee, H.; Tran, T.; Kim, B. C.; Rhee, W. J. *In situ* Simultaneous Detection of Surface Protein and microRNA in Clustered Extracellular Vesicles from Cancer Cell Lines Using Flow Cytometry. *ACS Biomater. Sci. Eng.* **2023**, *9*, 6369−6378.
(71) Guo, L. M.; Ding, G. F.; Xu, W. C.; Ge, H.; Jiang, Y.; Lu, Y. F. Anti-PD-L1 Antibody Enhances T Cell Immune Responses and Reduces Resistance of Breast Cancer Cells to Radiotherapy. *Oxid. Med. Cell. Longevity* **2022**, *2022*, No. 5938688.
(72) Zheng, X.; Dong, L.; Wang, K.; Zou, H.; Zhao, S.; Wang, Y.; Wang, G. MiR-21 Participates in the PD-1/PD-L1 Pathway-Mediated Imbalance of Th17/Treg Cells in Patients After Gastric Cancer Resection. *Ann. Surg. Oncol.* **2019**, *26*, 884−893.
(73) Bartel, D. P. MicroRNAs: Genomics, Biogenesis, Mechanism, and Function. *Cell* **2004**, *116*, 281−297.
(74) Jiang, T.; Hu, X.; Lin, C.; Xia, Z.; Yang, W.; Zhu, Y.; Xu, H.; Tang, H.; Shen, J. Rapid Visualization of Clostridioides Difficile Toxins A and B by Multiplex RPA Combined with CRISPR-Cas12a. *Front. Microbiol.* **2023**, *14*, No. 1119395.

https://doi.org/10.1021/acsnano.4c13557
ACS Nano 2025, 19, 1271−1285